

RESEARCH ARTICLE

10.1029/2018MS001440

Key Points:

- We compare TIME-GCM simulations of the 2010 sudden stratospheric warming (SSW) using specified dynamics (SD) and 4D Tendency nudging
- The 4D Tendency nudging is different than SD nudging as data-model differences are represented by a source term in the prognostic equations
- Selecting appropriate nudging parameters is important to accurately reproducing SSW induced thermosphere-ionosphere variability in TIME-GCM

Supporting Information:

- Supporting Information S1

Correspondence to:

M. Jones,
mcarthur.jones@nrl.navy.mil

Citation:

Jones, M. Jr., Drob, D. P., Siskind, D. E., McCormack, J. P., Maute, A., McDonald, S. E., & Dymond, K. F. (2018). Evaluating different techniques for constraining lower atmospheric variability in an upper atmosphere general circulation model: A case study during the 2010 sudden stratospheric warming. *Journal of Advances in Modeling Earth Systems*, 10, 3076–3102. <https://doi.org/10.1029/2018MS001440>

Received 16 JUL 2018

Accepted 18 NOV 2018

Accepted article online 22 NOV 2018

Published online 15 DEC 2018

©2018. The Authors.

This is an open access article under the terms of the Creative Commons Attribution-NonCommercial-NoDerivs License, which permits use and distribution in any medium, provided the original work is properly cited, the use is non-commercial and no modifications or adaptations are made. This article has been contributed to by US Government employees and their work is in the public domain in the USA.

Evaluating Different Techniques for Constraining Lower Atmospheric Variability in an Upper Atmosphere General Circulation Model: A Case Study During the 2010 Sudden Stratospheric Warming

McArthur Jones Jr.¹, Douglas P. Drob¹, David E. Siskind¹, John P. McCormack¹, Astrid Maute², Sarah E. McDonald¹, and Kenneth F. Dymond¹

¹Space Science Division, U.S. Naval Research Laboratory, Washington, DC, USA, ²High Altitude Observatory, National Center for Atmospheric Research, Boulder, CO, USA

Abstract We analyze the effects specified dynamics (SD) and 4D Tendency nudging have on accurately reproducing the middle and upper atmospheric variability induced by the 2010 sudden stratospheric warming (SSW) event in the National Center for Atmospheric Research thermosphere-ionosphere-mesosphere-electrodynamics general circulation model (TIME-GCM). TIME-GCM numerical experiments were performed using constrained middle atmospheric winds and temperatures from a high-altitude version of the Navy Global Environmental Model to compare the previously implemented SD scheme, with the newly implemented 4D Tendency scheme. Model comparisons focused on zonal mean winds, composition, planetary waves, and tides in the thermosphere-ionosphere system. Through 4D Tendency nudging we reveal that coupling coefficients of the one-way SD coupling approach between the TIME-GCM and *observed* SSW conditions were too strong. Prior implementations produced unusually strong vertical shears in the zonal mean winds in the mesosphere and lower thermosphere (MLT), where the model is free running. Differences in zonal mean MLT winds between SD and 4D Tendency nudging simulations resulted in migrating diurnal (DW1) and semidiurnal (SW2) tidal amplitude differences at lower thermospheric altitudes. The consequences of simulating different MLT dynamics using SD and 4D Tendency nudging in the overlaying ionosphere are reported and validated using electron density data from the Constellation Observing System for Meteorology, Ionosphere, and Climate satellites. Although we demonstrate that SD and 4D Tendency nudging techniques are approximately equivalent, results presented herein establish that 4D Tendency nudging has the added potential to identify physical model parameters that contribute to data-model differences during the 2010 SSW.

Plain Language Summary Understanding the meteorology of Earth's upper atmosphere on the time scales necessary to forecast *space weather* requires knowledge of the sources and propagation conditions of waves originating in the lower atmosphere, in addition to solar forcing. This principle underlies the ongoing effort in the middle and upper atmospheric modeling communities to replicate short-term variability of the mesosphere, thermosphere, and ionosphere associated with lower atmospheric phenomena that couple Earth's lower and upper atmosphere. Using a commonly used upper atmosphere general circulation model, this study demonstrates that the same model will produce different results in Earth's thermosphere and ionosphere depending on the technique employed to constrain model fields in the underlying middle atmosphere. Simulating different model ionospheres (and thermospheres) could have an important impact on the uncertainty associated with ionospheric forecasts used by communication and navigation users (e.g., Global Positioning System). We therefore evaluate two leading methods for constraining lower atmospheric variability in order to better understand the underlying assumptions associated with each. We show how these techniques, previously thought to be mathematically distinct, can be reconciled provided certain considerations are made about the strength of and the time constants associated with constraining an upper atmospheric general circulation model to reanalysis data.

1. Introduction

During the past two decades, and especially during the most recent solar minimum period, there has been a paradigm shift from a mainly solar forced upper atmosphere (e.g., thermosphere-ionosphere, TI) to an upper atmosphere that is also subjected to persistent terrestrial forcing from the lower atmosphere (Forbes et al., 2009; Mendillo et al., 2002; Rishbeth & Mendillo, 2001). It is now widely recognized that a major source of TI variability is driven by upward propagating atmospheric tides, gravity, and planetary waves, the origins of which lie in the troposphere and stratosphere (see reviews by Akmaev, 2011; England, 2012; Liu, 2016; Oberheide et al., 2015; Smith, 2012; Yiğit & Medvedev, 2015). The spatiotemporal variability driven by the waves and tides propagating up from below can be important for the *preconditioned* TI state (i.e., Pedatella & Liu, 2018; Thayer et al., 2012) and also comparable to the spatiotemporal variability associated with energy and particle deposition at high latitudes during geomagnetic storms (Hagan et al., 2015). Therefore, understanding the dominant mechanisms responsible for driving the dynamical, chemical, thermal, and electrodynamical variability in the TI across a wide range of spatiotemporal scales means fully resolving the relative roles between solar geomagnetic-driven variability and terrestrial-lower atmospheric-driven variability.

Recent advancements in middle and upper atmospheric modeling have led to self-consistent, coupled numerical models of the global stratosphere, mesosphere, thermosphere, and ionosphere that can generally incorporate the day-to-day variability in lower and middle atmospheric wave activity by constraining the relevant dynamical fields using observational and/or reanalysis data sets. Typically, observational data sets are incorporated into physics-based models through data assimilation (DA; e.g., Codrescu et al., 2018; Fuller-Rowell et al., 2004; Matsuo et al., 2012; Pedatella et al., 2018; Sutton, 2018; H. Wang et al., 2011, and references therein), while reanalysis data sets are incorporated into physics-based models via nudging. More formally nudging is referred to as Newtonian relaxation, where model fields are relaxed using a user-specified time constant (e.g., Liu et al., 2013; Marsh, 2011; Smith, Pedatella, et al., 2017; Siskind & Drob, 2014; J. C. Wang et al., 2017, and references therein). Constrained numerical modeling has become an essential tool for interpreting the observed short-term (i.e., days to weeks) TI variability, especially in response to sudden stratospheric warming (SSW) events. For example, Pedatella et al. (2014) and Pedatella, Fang, et al. (2016) demonstrated that differences in the simulated TI variability during the 2009 SSW period in four whole atmosphere and TI models were driven by different model representations of the zonal mean background atmosphere, planetary waves, and semidiurnal tides. Pedatella et al. (2014) mostly attributed these model differences in short-term TI zonal mean, tidal, and planetary wave variability to differences in the gravity wave parameterizations between all the models. Their results also suggest that model differences not only are a consequence of different model physics but could also result from the different nudging schemes, different nudging data sources (i.e., different reanalysis products), and different altitudes constrained in their model simulations. Thus, this study focuses on understanding how different nudging techniques influence model simulations within and outside the region where the model is constrained by reanalysis data, which have important implications for how one interprets their model results.

A commonly used nudging technique in middle and upper atmospheric global modeling is generally referred to as *specified dynamics* (SD). Marsh (2011) first employed this in the National Center for Atmospheric Research (NCAR) Whole Atmosphere Community Climate Model (WACCM) series of models (referred to in the literature as SD-WACCM or SD-WACCM-X, where the X refers to the TI extension), where model winds and temperatures are constrained at each model time step and relaxed toward *observed* winds and temperatures. Different implementations of SD nudging have been reported (e.g., the NCAR thermosphere-ionosphere-mesosphere-electrodynamics general circulation model [TIME-GCM] by Liu et al., 2013), but to date the differing effects on model physics have not been quantified. Maute et al. (2015) reported zonal mean zonal wind discontinuities in the low-latitude mesopause region when trying to reproduce the January 2013 SSW event in the SD constrained TIME-GCM nudged by SD-WACCM-X simulations up to ~96 km. In turn, WACCM-X was constrained by the Goddard Earth Observing System Data Assimilation System Version 5 (GEOS-5; Rienecker et al., 2008) operational version up to 40 km. They found that constraining the TIME-GCM only up to ~96 km resulted in strong eastward gravity wave drag (GWD). To ameliorate the unintended side effects associated with this increased GWD, Maute et al. (2015) raised the vertical extent of their nudging from ~96 to ~110 km (i.e., a region where GWD is less important to the zonal wind balance). Smith, Pedatella, et al. (2017) demonstrated model error growth away from the observed atmospheric state (i.e., which was assumed to be a prior free-running WACCM simulation) depended on the vertical extent and frequency of the data used to constrain wind and temperature fields, as well as the method used for representing GWD in SD-WACCM.

J. C. Wang et al. (2017) also employed SD nudging in the TIME-GCM to study the quasi-2-day planetary wave over five different boreal winters (e.g., January and February 2005, 2006, and 2008–2010) and found similar zonal mean zonal wind discontinuities at low latitudes to those displayed in Maute et al. (2015).

A somewhat different nudging approach was used by Siskind and Drob (2014) and Siskind et al. (2014) to investigate how nonmigrating tides affect the vertical transport of light constituents in the TI. They employed a nudging technique in the NCAR thermosphere-ionosphere-electrodynamics general circulation model (TIE-GCM) pioneered by the mesoscale modeling community (cf., Stauffer & Seaman, 1990, 1994). The Stauffer and Seaman (1990, 1994) nudging approach relaxes the model state toward the observed state by adding one or more artificial tendency terms to the right-hand side of the prognostic model equations based on the difference between the two states guided by a user-specified time constant. Stauffer and Seaman (1990) and Jeuken et al. (1996) offer some details on the impact the Stauffer and Seaman (1990, 1994) nudging technique has on the parameterized physics in the troposphere and stratosphere, but the connection between the Stauffer and Seaman (1990, 1994) nudging scheme and parameterized physics has not been studied with respect to the TI system. Addressing this issue is a major goal of the present paper.

In this report we evaluate in detail the impact that SD nudging and the Stauffer and Seaman (1990, 1994) nudging technique (hereafter referred to as *4D Tendency* nudging, where the 4D denotes three dimensions in space and one in time) have on short-term TI variability. For this purpose, we performed a set of numerical experiments with the TIME-GCM that constrain the meteorological fields in the stratosphere and mesosphere using NAVGEM-HA (Navy Global Environmental Model a high-altitude version; McCormack et al., 2017), during the 2010 boreal winter months that covers the 2010 SSW period from mid-January to mid-February. TIME-GCM simulations constrained by NAVGEM-HA winds and temperatures based on the SD nudging methodologies described by Maute et al. (2015; hereafter referred to as SD_{zm}) and J. C. Wang et al. (2017; hereafter referred to as SD_{full}) are presented and compared with those that employed the 4D Tendency nudging technique (hereafter referred to as *4D Tend*).

Comparisons between the SD_{zm} , SD_{full} , and 4D Tend TIME-GCM simulations allow us to isolate and quantify the effects that different nudging schemes have on simulating the variability in the TI system, without having to worry about different model physics or nudging data sources. Through force term analysis of the momentum equations in our TIME-GCM simulations we explain how the different nudging techniques result in different model representations of zonal mean winds and wave perturbations in the mesosphere and thermosphere. We also examine the consequences that different nudging schemes can have on atomic oxygen (O) in the thermosphere and electron density in the ionosphere, validating our ionospheric calculations against available Constellation Observing System for Meteorology, Ionosphere, and Climate (COSMIC) radio occultation measurements. We lastly demonstrate how the SD and 4D Tendency nudging techniques are *effectively* equivalent for zonal mean and large-scale dynamics and can be used to guide their proper implementation in middle and upper atmospheric models. The modeling results presented herein demonstrate that 4D Tendency nudging can track the spatial distribution and time history of data-model wind and temperature differences, accounting for and even identifying limitations in model physics, which is important for future middle and upper atmosphere modeling improvements. Finally, while our specific context is the 2010 SSW, we will suggest that our results are representative for a broader range of simulated mesosphere and lower thermosphere (MLT) and TI dynamics.

2. Model Simulations, Data Sets, and Methodology

2.1. TIME-GCM

The NCAR TIME-GCM is one of several NCAR global GCMs of the middle and upper atmosphere. It self-consistently (Roble, 1995; Roble & Ridley, 1994) solves the momentum, energy, continuity, and electrodynamic equations from first principles for the global circulation, temperature, composition, and electrodynamics of the mesosphere and TI on a regular grid in spherical coordinates in longitude and latitude, and log pressure in the vertical assuming hydrostatic balance. The horizontal resolution of the TIME-GCM is $2.5^\circ \times 2.5^\circ$ (longitude \times latitude) and four grid points per vertical scale height, extending from ~ 12 hPa to $\sim 4.6 \times 10^{-10}$ hPa (or ~ 30 km to ~ 450 – 600 km depending on solar cycle conditions). Solar forcing is specified following the solar irradiance parameterization presented by Solomon and Qian (2005), where the solar irradiance spectrum is scaled by the extreme ultraviolet flux model for aeronomic calculations model (Richards et al., 1994). Geomagnetic forcing is parameterized by specifying hemispheric power (after Evans, 1987) and cross-polar cap potential or using a 3-hourly K_p proxy after Emery et al. (2012) with empirical high-latitude ion convection

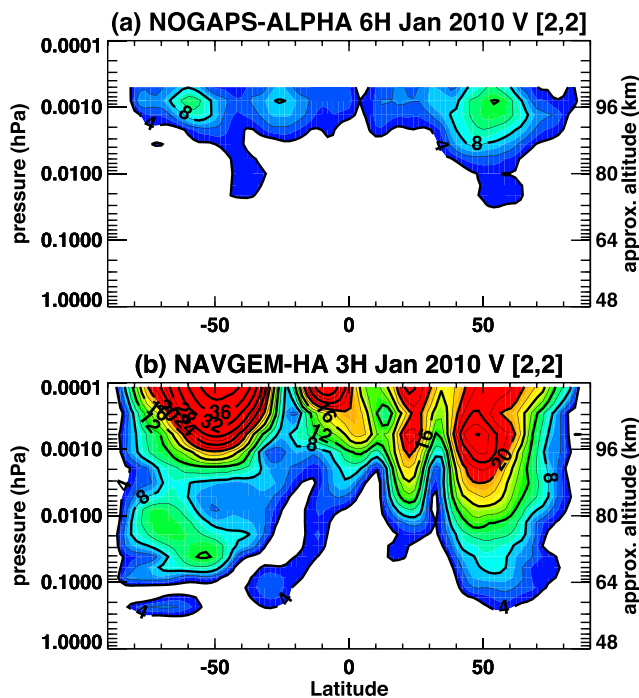


Figure 1. Monthly mean migrating (i.e., westward propagating) semidiurnal tide with zonal wave number 2 (given by $[n, s]$ or $[2, 2]$, where n is the subharmonic of a solar day and s is zonal wave number) meridional wind amplitudes as a function of latitude and pressure for January 2010 derived from (a) 6-hourly NOGAPS-ALPHA analyses and (b) 3-hourly NAVGEM-HA analysis/forecast fields. The vertical axis on right illustrates approximate altitude in log pressure coordinates. Bold contours are drawn every 4 m/s and thin contours every 2 m/s. NOGAPS-ALPHA = NOGAPS-ALPHA Navy Operational Global Atmospheric Prediction System-Advanced Level Physics High Altitude forecast model; NAVGEM-HA = Navy Global Environmental Model a high-altitude version.

ability in whole atmosphere models (e.g., McDonald et al., 2018). Unlike the earlier NOGAPS-ALPHA system, which used a three-dimensional variational (3DVAR) DA algorithm that consolidates observations within a 6-hr window and used static model covariance estimates, the hybrid 4DVAR NAVDAS-AR in NAVGEM-HA accounts for time-varying observations within the 6-hr window through a linear combination of climatological covariances and ensemble-based model covariances to obtain more realistic estimates of forecast model uncertainties within the DA algorithm. The NAVGEM-HA system was recently validated by McCormack et al. (2017) with multiple independent ground-based medium frequency radar wind observations over the 2009–2010 and 2012–2013 Northern Hemisphere winters.

The DA component of NAVGEM-HA produces global synoptic analyses of key meteorological variables (e.g., winds, temperature, geopotential height, water vapor, and ozone) every 6 hr (00, 06, 12, and 18 UTC), which are then used to initialize short-term forecasts to produce a combined 3-hourly analysis/forecast product each day. The advantage of this 3-hr cadence is that it allows for a better representation of the semidiurnal tide. This is demonstrated in Figure 1, which compares the meridional and vertical structure of monthly mean migrating semidiurnal tidal amplitudes in meridional wind for January 2010 derived from 3-hourly NAVGEM-HA output and 6-hourly NOGAPS-ALPHA output. The NAVGEM-HA results show much larger amplitudes of the migrating semidiurnal tide compared to NOGAPS-ALPHA and are in good agreement with migrating semidiurnal tidal amplitude estimates from Thermosphere Ionosphere Mesosphere Energetics and Dynamics (TIMED) Doppler Interferometer (TIDI) reported by Wu and Nozawa (2015; see Figure 7) during January 2010. This indicates that the analysis frequency of the constraining data set is important, especially in generating the pertinent features (i.e., tidal perturbations with periods less than 24 hr) responsible for much of the TI variability during SSW events (e.g., Pedatella & Liu, 2013; Pedatella, Richmond, et al., 2016, and references therein). Furthermore,

and particle precipitation derived from Heelis et al. (1982) and Roble and Ridley (1987), respectively. The electrodynamics component of the model uses the International Geomagnetic Reference Field (Richmond, 1995; Richmond et al., 1992). Subgrid-scale gravity waves are parameterized in the TIME-GCM using a modified Lindzen (1981) scheme that includes molecular damping effects in the MLT (see J. C. Wang et al., 2017; Yamashita et al., 2010, for more details). The reader is referred to Roble (1996), Qian et al. (2014), and Richmond and Maute (2014) for details on the historical development of the NCAR TI GCMs.

Of specific interest for this work is the lower boundary forcing. Typically, the model is driven at the lower boundary with zonal and daily averaged European Centre for Medium-Range Weather Forecasts (ECMWF) reanalysis data and climatological tidal perturbations from the Global Scale Wave Model (GSWM Hagan & Forbes, 2002, 2003). With this approach Maute et al. (2014) demonstrated that the TIME-GCM could successfully replicate the 2006 SSW in the middle and upper atmosphere. However, Maute et al. (2015) later reported problems in simulating the 2010 SSW period by simply forcing the model with realistic meteorological conditions solely at the lower boundary. They instead suggested constraining the dynamical and temperature structure of the stratosphere and mesosphere via nudging to reanalysis data during the boreal winter months of 2010.

2.2. NAVGEM-HA

NAVGEM-HA is a prototype high-altitude numerical weather prediction system designed to study the meteorology of the lower and middle atmosphere from the surface to ~100 km. NAVGEM-HA replaces the earlier Navy Operational Global Atmospheric Prediction System-Advanced Level Physics High Altitude forecast model (NOGAPS-ALPHA; Eckermann et al., 2009). NAVGEM-HA combines a semi-implicit semi-Lagrangian global forecast model (Hogan et al., 2014) with a hybrid four-dimensional variational (4DVAR) DA system based on the Naval Research Laboratory Atmospheric Variational Data Assimilation System-Accelerated Representer (NAVDAS-AR, Kuhl et al., 2013, and references therein) and has been used to constrain the tropospheric, stratospheric, and mesospheric vari-

this suggests that the analysis frequency will play an important role in accurately simulating (and forecasting) space weather, similar to the impacts it can have on accurately reproducing vertical transport of lower stratospheric composition (e.g., Monge-Sanz et al., 2013; Pawson et al., 2007).

In order to facilitate implementation of both nudging schemes in the TIME-GCM, NAVGEM-HA temperature and horizontal wind fields were interpolated in both space and time from the NAVGEM-HA Gaussian $1^\circ \times 1^\circ$ resolution (longitude \times latitude) grid to the TIME-GCM's equally spaced $2.5^\circ \times 2.5^\circ$ grid in spherical coordinates. For this the vector spherical harmonic transform projection method described by Adams and Swartrauber (1999) and Swartrauber and Spatz (2000) was utilized. Over the study interval the 3-hourly NAVGEM-HA fields are first transformed in the horizontal dimension then linearly interpolated from NAVGEM-HA pressure surfaces to TIME-GCM pressure surfaces and the lower boundary. This is performed once and stored for multiple TIME-GCM nudging numerical experiments. During TIME-GCM model integration the mapped 3-hourly NAVGEM-HA fields are linearly interpolated to each TIME-GCM time step.

2.3. SD Nudging in the TIME-GCM

SD nudging in the TIME-GCM was first implemented by Liu et al. (2013) to study the short-term ionospheric variability forced by lower atmospheric waves. Maute et al. (2015) and J. C. Wang et al. (2017) provided the most detailed descriptions of the effects SD nudging has on TIME-GCM dynamics. The SD nudging approaches of Maute et al. (2015) and J. C. Wang et al. (2017) were slightly different, but both constrained TIME-GCM horizontal winds and neutral temperatures in an effort to study the lower atmospheric driving of the MLT and TI. Maute et al. (2015) constrained the zonal mean background atmosphere in the TIME-GCM using hourly SD-WACCM-X output (i.e., WACCM-X-L116 was constrained using GEOS-5), such that the zonal mean horizontal winds and neutral temperatures take the following form in the momentum and thermodynamic energy equations:

$$\bar{X}(\theta, z, t) = (1 - \alpha\zeta(z))\bar{X}_{\text{Model}}(\theta, z, t) + \alpha\zeta(z)\bar{X}_{\text{Data}}(\theta, z, t), \quad (1)$$

where θ = latitude, $z = \ln \frac{p_0}{p}$ or log pressure level ($p_0 = 5 \times 10^{-7}$ hPa), t = time, \bar{X} represents zonal mean zonal (\bar{u}), and meridional (\bar{v}) winds, and the zonal mean temperature (\bar{T}) from TIME-GCM (\bar{X}_{Model}) and WACCM-X-L116/GEOS5 (\bar{X}_{Data}), where the overbar represents a zonal average dynamical field. The fraction, α , is used to determine the relaxation time following Smith, Pedatella, et al. (2017), which in the Maute et al. (2015) case is assumed to be 1. As described by Smith, Pedatella, et al. (2017), $\alpha = 1$ means that model fields are overwritten by observed fields at each model time step (Δt) and do not enter the prognostic equation weighted against model calculated tendency terms, as is the case when $\alpha < 1$. Thus, in the SD_{zm} case, the TIME-GCM zonal mean horizontal winds and temperatures are relaxed to *observations* at every model time step with a relaxation time of 30 s at the model lower boundary, and decreases away from the lower boundary in the vertical following the vertical weighting function ($\zeta(z)$).

Essentially, this vertical weighting function $\zeta(z)$ determines how strongly the model and data source (in Maute et al., 2015, case WACCM-X-L116/GEOS5) are coupled as a function of pressure (altitude). For the Maute et al. (2015) case,

$$\zeta(z) = \cos^2 \left[\frac{\pi}{2} \left(\frac{z - z_{\text{lb}}}{z_{\text{max}} - z_{\text{lb}}} \right) \right], \quad (2)$$

where z_{lb} is the lower boundary log pressure level (-17 at ~ 30 km) and z_{max} is the log pressure level above which the TIME-GCM becomes free running. Figure 2 (black line) shows $\zeta(z)$ from the SD_{zm} case, where the TIME-GCM background atmosphere is constrained using WACCM-X-L116/GEOS5 fields starting at z_{lb} up to $z_{\text{max}} = -5$ (or ~ 110 km). Maute et al. (2015) also prescribed tides and planetary waves at the TIME-GCM lower boundary from WACCM-X-L116/GEOS5. Originally, Maute et al. (2015) invoked an upper nudging boundary of $z_{\text{max}} = -7$ (~ 96 km) but found that this resulted in strong vertical gradients in the low-latitude zonal mean zonal winds around $z = -7$, due to increased GWD. Therefore, Maute et al. (2015) raised z_{max} from -7 to -5 where gravity wave forcing was reduced to insure lower atmospheric tides and planetary waves propagated through a realistic background atmosphere.

Later, J. C. Wang et al. (2017) employed the SD nudging technique on both the zonal mean and wave perturbations (i.e., the full dynamical fields) in TIME-GCM. J. C. Wang et al. (2017) constrained the full dynamical model fields using hourly NOGAPS-ALPHA forecasts (see Siskind et al., 2012, for more details), including longitude (λ) in equation (1) written as

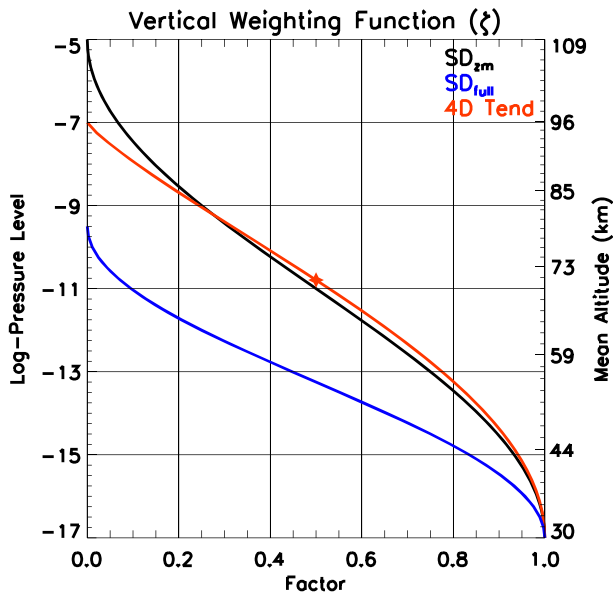


Figure 2. Vertical weighting function $\zeta(z)$, as function of log pressure level in the TIME-GCM used in Maute et al. (2015) (denoted SD_{zm} , black line), J. C. Wang et al. (2017) (denoted SD_{zm} , blue line), and the TIME-GCM simulations performed herein (denoted 4D Tend, red line). Shown on the right vertical axis is the global mean geometric altitude of the log pressure levels. The red asterisk represents the midpoint or where $\zeta = 0.5$ (roughly log pressure level -10.8 or ~ 70 km) in the 4D Tend case, above (below) which the nudging term is more weighted toward the model (data) dynamical fields. TIME-GCM = thermosphere-ionosphere-mesosphere-electrodynamics general circulation model; SD = specified dynamics.

$$X(\lambda, \theta, z, t) = (1 - \alpha\zeta(z))X_{\text{Model}}(\lambda, \theta, z, t) + \alpha\zeta(z)X_{\text{Data}}(\lambda, \theta, z, t), \quad (3)$$

where $X(\lambda, \theta, z, t) = \bar{X}(\theta, z, t) + X'(\lambda, \theta, z, t)$, and X_{Model} (X_{Data}) represents u , v , and T from TIME-GCM (NOGAPS-ALPHA). J. C. Wang et al. (2017) assumed $\alpha = 1$ and a Δt of 30 s. J. C. Wang et al. (2017) also used the same functional form of $\zeta(z)$ as Maute et al. (2015), except with $z_{\text{max}} = 6 \times 10^{-3}$ hPa (or approximately log pressure level -9.5). At the lower boundary $\zeta(z) = 1$ and the TIME-GCM fields are replaced with NOGAPS-ALPHA fields. While J. C. Wang et al. (2017) allowed the TIME-GCM to be free running above ~ 80 km (see blue line in Figure 2, which was lower than ; Maute et al., 2015), they also reported zonal mean zonal wind discontinuities at low latitudes. J. C. Wang et al. (2017) attributed this zonal mean zonal wind discontinuity to differences between the gravity wave parameterizations used in TIME-GCM and NOGAPS-ALPHA.

In summary, Maute et al. (2015) and J. C. Wang et al. (2017) both employed SD nudging in the TIME-GCM but with slightly different characteristics including zonal mean field nudging versus full field nudging, WACCM-X-L116/GEOS5 versus NOGAPS-ALPHA data sources, and altitudes of constraints of ~ 110 versus ~ 80 km. However, both Maute et al. (2015) and J. C. Wang et al. (2017) SD nudging TIME-GCM simulations yielded the same anomalous zonal mean artifacts in the low-latitude MLT. Resolution of this nudging-induced artifact lies in independently testing the SD_{zm} and SD_{full} approaches assuming exactly the same data sources and vertical nudging structure in the TIME-GCM and comparing those results against another nudging technique.

2.4. Four-Dimensional Tendency Nudging in the TIME-GCM

Four-dimensional Tendency nudging (originally called 4D DA by Stauffer & Seaman, 1990, 1994, and references therein) was developed for tropospheric mesoscale weather prediction and was applied to the TI system by

Siskind and Drob (2014) and Siskind et al. (2014). Conceptually, 4D Tendency nudging dynamically adjusts model horizontal winds and temperatures to reanalysis data (or observations in the case of DA) by adding an artificial source term to the prognostic zonal, meridional, and thermodynamic energy equations. The correction term is proportional to the difference between the modeled and observed states. In this manner, the nudging process acts as a representative proxy for the unresolved model processes, including underlying biases in the free-running model configuration and uncertainties in the parameterized model physics.

Following the mathematical formulations presented in Jeuken et al. (1996) and Telford et al. (2008) for lower atmospheric GCMs, the relaxation of an atmospheric variable, X , to the observed state is written as

$$\frac{\partial X(\lambda, \theta, z, t)}{\partial t} = F_{\text{Model}}(X(\lambda, \theta, z, t)) + G\zeta(z) t_{\text{weight}}(t) (X_{\text{Model}}(\lambda, \theta, z, t) - X_{\text{Data}}(\lambda, \theta, z, t)), \quad (4)$$

where X_{Model} can be, for example, TIME-GCM horizontal winds and or neutral temperatures. $F_{\text{Model}}(X)$ represents model tendency terms (e.g., advection, pressure gradient, and GWD) in the u , v , and T conservation equations, and the entire second term is the relaxation term (artificial tendency term) whose magnitude is proportional to $G[s^{-1}]$, the relaxation factor. Note that 4D Tendency nudging is different than the dynamic initialization technique discussed in Song et al. (2018), as it does not include the local time rate of change of observed winds and temperatures in the artificial tendency term. The time weighting function (t_{weight}) ensures a gradual transition from an initial model state driven with lower boundary forcing and or dynamical constraints to a model state that is driven by a different lower boundary or dynamical constraints and to mitigate spurious artifacts that could arise during model spin-up (see the supporting information and Figure S1 for more details).

One distinguishing characteristic of 4D Tendency nudging is that it accounts for data-model differences on the right-hand side of the prognostic equations, where Maute et al. (2015) and J. C. Wang et al. (2017) SD-like approaches correct the prognostic variables of interest prior to model calculations of important dynamical processes (including advection and pressure gradients). Thus, the 4D Tendency nudging approach allows

Table 1
Nomenclature for TIME-GCM Simulations

Label	Reference	Nudging scheme	Relaxation factor (G)	α
ECMWF + GSWM (driven)	Maute et al. (2014)	N/A—Driven at model lower boundary only	—	—
SD_{zm}	Maute et al. (2015)	SD—zonal mean (equation (1))	—	1
SD_{full}	J. C. Wang et al. (2017)	SD—full field (equation (3))	—	1
4D Tend	This paper	4D Tendency (equation (4))	$1.5 \times 10^{-4} \text{ s}^{-1}$	—

Note. TIME-GCM = thermosphere-ionosphere-mesosphere-electrodynamics general circulation model; ECMWF = European Centre for Medium-Range Weather Forecasts; GSWM = Global Scale Wave Model; N/A = not available.

for trade-offs between the specified observed dynamical state and the dynamical state of the model, while maintaining physical self-consistency (including nonlinear feedbacks and model filtering) with the rest of the model physics, assuming the user-specified choice of relaxation is appropriate. For example, a G that is too small will be ineffective at constraining model dynamical fields, and a G that is too large will cause the model to produce spurious artifacts. The effects of choosing different relaxation factors are discussed in section 4 where the approximate relationship between 4D Tendency nudging and SD nudging relaxation time constants is examined.

2.5. TIME-GCM Simulations

To isolate the effects of SD and 4D Tendency nudging schemes on MLT and TI dynamics and composition during the 2010 SSW period (i.e., 3 December 2009 to 21 March 2010), we performed three otherwise identical TIME-GCM simulations. The time step (Δt) for all simulations was 30 s, and the lower boundary conditions (i.e., zonally and diurnally averaged fields plus tides in u , v , T , and geopotential heights) were specified at log pressure level -17 using 3-hourly NAVGEM-HA output from McCormack et al. (2017). In all cases, we used observed external solar and geomagnetic forcing, including daily varying and 81-day averaged $F_{10.7}$ and 3-hourly Kp to parameterize the high-latitude forcing, as described above in section 2.1. The differences between these three initial TIME-GCM simulations are summarized in Table 1. The SD_{zm} (SD_{full}) simulation is designed to diagnose the SD nudging approach of Maute et al. (2015) (J. C. Wang et al., 2017); that is, TIME-GCM zonal mean (full field) horizontal winds and neutral temperatures are constrained using 3-hourly NAVGEM-HA zonal mean (full) fields in stratosphere and mesosphere following equation 1 (3). Here α is equal to 1 in both the SD_{zm} and SD_{full} TIME-GCM simulations resulting in a model relaxation time of 30 s. The 4D Tend simulation is representative of the 4D Tendency nudging approach, where TIME-GCM zonal mean and wave perturbations in horizontal winds and neutral temperatures are relaxed to 3-hourly NAVGEM-HA fields in the middle atmosphere via equation (4). For the 4D Tend case, G is chosen to be $1.5 \times 10^{-4} \text{ s}^{-1}$, corresponding to a relaxation time of ~ 1.85 hr (after Siskind & Drob, 2014; Siskind et al., 2014). Additionally, we performed a *standard/driven* TIME-GCM simulation for reference, driven solely at the lower boundary by daily varying background fields from ECMWF reanalysis data and climatological migrating and nonmigrating diurnal and semidiurnal tidal perturbations the GSWM version 2009 (Zhang et al., 2010a, 2010b). Note that the ECMWF + GSWM simulation (see Table 1) is *not* constrained by NAVGEM-HA fields in the middle atmosphere and is only forced at the lower boundary above which the model free running.

To minimize any differences in the vertical weighting distribution of the NAVGEM-HA nudging the SD_{zm} , SD_{full} , and 4D Tend, TIME-GCM simulations all invoked a $\zeta(z)$ given by

$$\zeta(z) = \cos^{1.2} \left[\frac{\pi}{2} \left(\frac{z - z_{lb}}{z_{max} - z_{lb}} \right) \right], \quad (5)$$

or the red curve in Figure 2 (labeled 4D Tend), where $z_{lb} = -17$ (or ~ 30 km) and $\zeta(z) = 1$, while $z_{max} = -7$ (or ~ 96 km) where $\zeta(z) = 0$. For reference, $\zeta = 0.5$ occurs at roughly 70 km (or ~ 0.025 hPa) above which the nudging term is more weighted toward TIME-GCM dynamical fields than reanalysis dynamical fields. Additionally, above ~ 85 km (or ~ 0.003 hPa), $\zeta \leq 0.2$, implying that the TIME-GCM dynamical fields are only weakly constrained by the NAVGEM-HA dynamical fields. A potential difference from the original SD_{zm} and SD_{full} TIME-GCM simulations is that in our simulations the 3 December to 31 December 2009 were used as model spin-up. Specifically, we utilized a logistic function to smoothly transition from a TIME-GCM initial state driven by ECMWF and GSWM09 lower atmospheric forcing to a TIME-GCM initial state *driven* by NAVGEM-HA lower

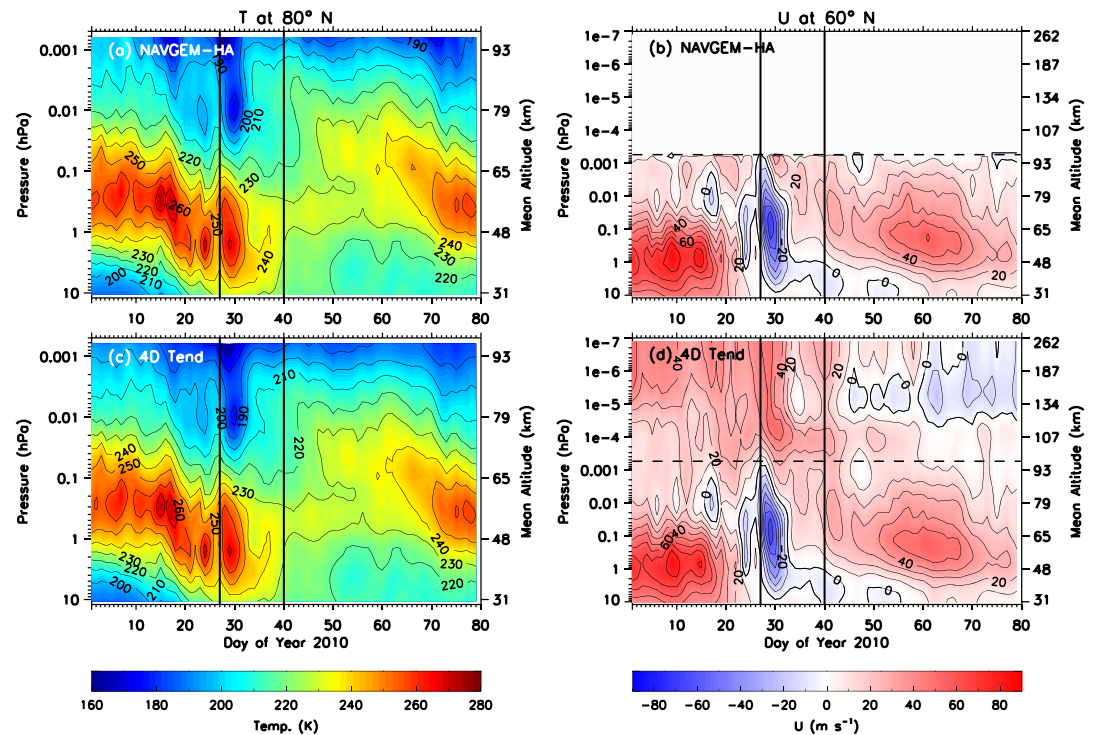


Figure 3. Zonal and diurnal mean temperatures at 80°N geographic latitude (a, c) and zonal and diurnal mean zonal winds at 60°N geographic latitude (b, d) simulated by NAVGEM-HA (a and b) and TIME-GCM nudged by NAVGEM-HA using the 4D Tend nudging approach (4D Tend, c and d) from 1 January to 21 March 2010. Values along the abscissa represent day of the year in 2010 or days since 1 January 2010. The black vertical line at 27 January 2010 (9 February 2010) denotes the onset of persistent mesospheric wind reversals at 60°N after McCormack et al. (2017), (traditional onset of a major sudden stratospheric warming, that is, zonal wind reversal at 60° and 10 hPa). Dashed black horizontal lines represent the z_{\max} log pressure level. Contours are shown every 10 K and ± 10 m/s. NAVGEM-HA = Navy Global Environmental Model a high-altitude version.

and middle atmospheric forcing with an inflection point of 5 days (see the supporting information and Figure S1 for more details). This follows from the concepts also employed by the mesoscale modeling community whereby a time ramp is used to avoid shocking the model physics, which can occur when constraining to observations too quickly. Following the conclusions of Siskind et al. (2014) and to be consistent with prior TIME-GCM simulations performed by J. C. Wang et al. (2017), the eddy diffusion coefficient (K_{zz}) in all our TIME-GCM simulations was reduced by a factor of 10 (i.e., approximately an order of magnitude lower than the global average values reported by Jones et al., 2017) in order to compensate for the increased mixing downward transport introduced by including realistic wave perturbations from NAVGEM-HA.

3. Results

3.1. The 2010 SSW Period

Since McCormack et al. (2017) demonstrated that NAVGEM-HA reproduces the middle atmospheric dynamical signatures associated with the 2010 SSW (and independently validated their results using meteor radar data), we first compare our different TIME-GCM simulations constrained by NAVGEM-HA dynamical fields to those produced by NAVGEM-HA during the boreal winter months of 2010. Figure 3 depicts the zonal and diurnal mean temperature and zonal winds at 80°N and 60°N, respectively, from NAVGEM-HA (a and b) and the 4D Tend TIME-GCM simulation (c and d) in January–March 2010. Figure 3 only shows the 4D Tend simulation, while analogous temperature and wind results for the SD_{zm} and SD_{full} simulations are shown in Figure S2 in the supporting information since the three different TIME-GCM simulations only exhibit small differences at high latitudes. Note that the vertical extent of zonal mean temperatures shown in Figures 3a and 3c are limited to the constrained region of the TIME-GCM (see Figure 2), while the zonal mean zonal winds extend up to 1×10^{-7} hPa (the dashed line denoting where the model is free running). Two black vertical lines are shown in each panel. They mark two key dates in the 2010 SSW event. The rightmost, on 9 February 2010 (day of year

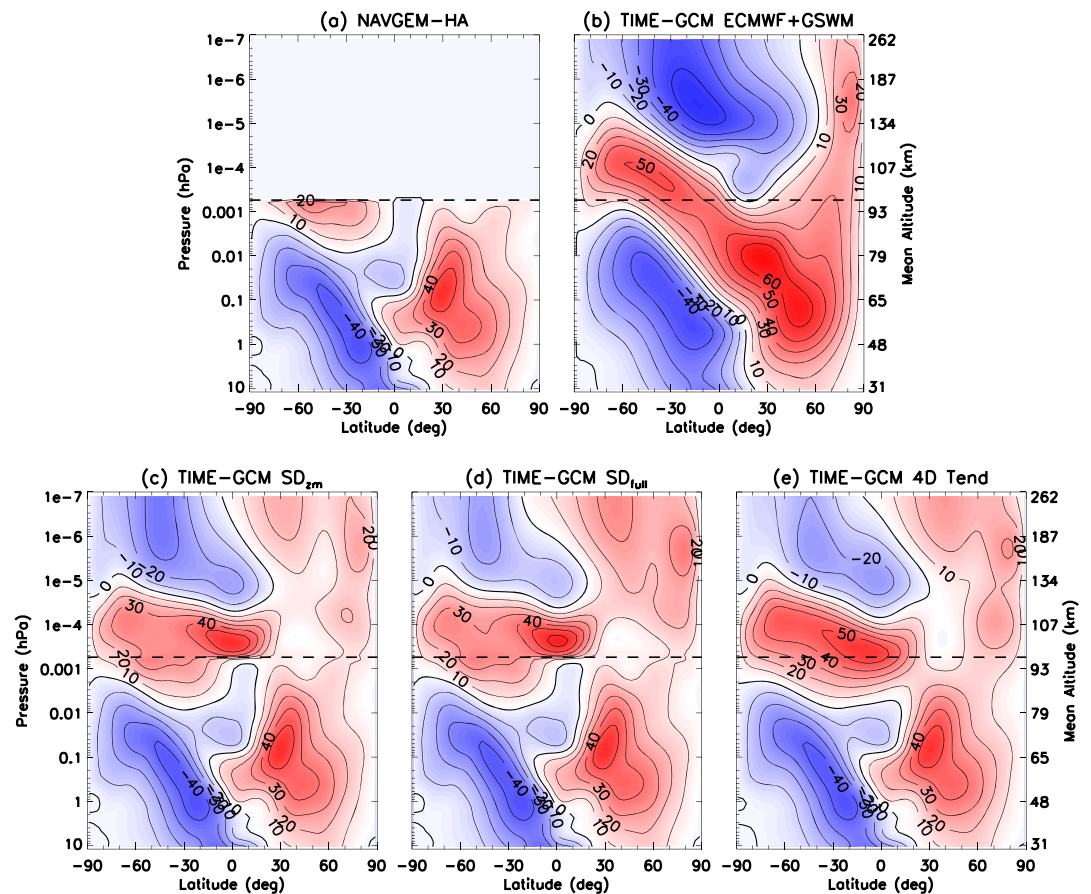


Figure 4. Zonal mean zonal winds averaged from 1 January to March 21 2010 as a function of latitude and pressure/mean altitude simulated by NAVGEM-HA (a), TIME-GCM ECMWF+GSWM (driven, b), TIME-GCM SD_{zm} (c), TIME-GCM SD_{full} (d), and TIME-GCM 4D Tend (e). The bold dashed line indicates where $\zeta = 0$, below (above) which the TIME-GCM is constrained (free running) in the different nudging simulations. Contours are shown every ± 10 m/s. NAVGEM-HA = Navy Global Environmental Model a high-altitude version; TIME-GCM = thermosphere-ionosphere-mesosphere-electrodynamics general circulation model; ECMWF = European Centre for Medium-Range Weather Forecasts; GSWM = Global Scale Wave Model; SD = specified dynamics.

40), corresponds to the classically defined date of the onset of a major SSW, that is, the reversal of the zonal mean zonal winds from eastward to westward at 60°N and 10 hPa (Butler et al., 2015). However, as McCormack et al. (2017) point out, for these events, a sustained (>5 days) reversal of the mesospheric zonal winds at 60°N typically precedes the stratospheric reversal. This is marked by the vertical line at 27 January 2010 (day of year 27).

The 4D Tend (Figure 3c) TIME-GCM simulation reproduces the middle atmospheric zonal mean temperature characteristics of the 2010 SSW commensurate with NAVGEM-HA zonal mean temperatures at 80°N , capturing the descent of the stratopause beginning near day 18 and subsequent stratospheric warming. The latitude-altitude structure of the zonal mean zonal winds at 60°N from NAVGEM-HA and the 4D Tend simulation (Figures 3b and 3d) also compare quite well, with all the TIME-GCM simulations (including SD_{zm} and SD_{full} in Figure S2) reproducing the sustained mesospheric and stratospheric zonal wind reversals. Thus, the overall representation of the 2010 SSW at high latitudes is generally consistent between the three TIME-GCM simulations and NAVGEM-HA. This, however, is not the case at lower latitudes and is the focus of the subsequent discussion.

3.2. Zonal Mean Winds

The short-term variability in the TI resulting from SSWs is mainly attributed to variability in upward propagating waves, the structures of which are dependent upon the zonal mean wind field of the middle and upper atmosphere through which they propagate (Forbes & Vincent, 1989; Jin et al., 2012; Lindzen & Hong, 1974).

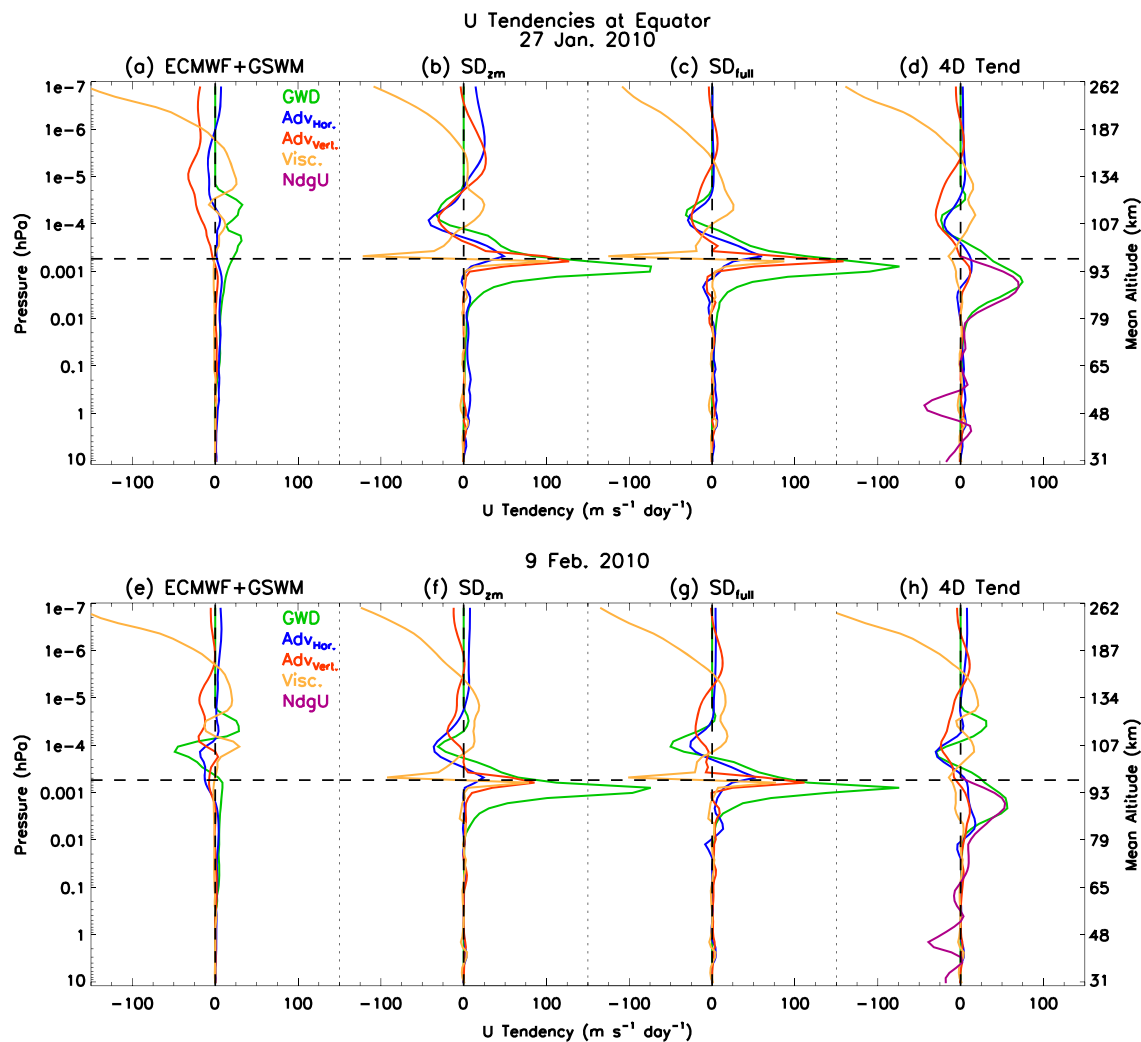


Figure 5. Daily averaged zonal mean zonal wind tendencies at the equator as a function of pressure/mean altitude on 27 January 2010 (day of year 27) and 9 February 2010 (day of year 40) from the TIME-GCM ECMWF + GSWM (driven, a and e), SD_{zm} (b and f), SD_{full} (c and g), and 4D Tend (d and h) cases. The tendencies shown are GWD (green), horizontal advection ($Adv_{Hor.}$, blue), vertical advection ($Adv_{Vert.}$, red), vertical viscosity (Visc., orange), and in the 4D Tend case the artificial nudging tendency term (NdgU, purple). The bold dashed line indicates where $\zeta = 0$, below (above) which the TIME-GCM is constrained (free running) in the different nudging simulations. ECMWF = European Centre for Medium-Range Weather Forecasts; GSWM = Global Scale Wave Model; SD = specified dynamics; GWD = gravity wave drag.

To systematically evaluate the effect that the SD_{zm} , SD_{full} , and 4D Tend nudging schemes have on the zonal mean zonal winds in the TIME-GCM, Figure 4 shows the simulated zonal and diurnal mean zonal winds averaged from 1 January to 21 March 2010. Also shown for reference is the TIME-GCM simulation driven at the model lower boundary by ECMWF zonal means and planetary waves and GSWM tides at the (see Table 1). The comparisons between the nudged cases in Figure 4 (Figures 4c–4e) with the driven case (Figure 4b) serve to illustrate the difficulty that the TIME-GCM has in simulating mesospheric dynamics without being constrained in the mesosphere.

Figure 4 clearly shows the key differences in mesospheric zonal winds between the four TIME-GCM simulations, specifically at tropical latitudes above ~ 0.01 hPa. While SD_{zm} and SD_{full} reproduce the NAVGEM-HA winds up to the top nudging level, they then both reveal a very sharp jump in the winds to a strong (>50 m/s) eastward jet immediately above. This sharp vertical gradient was also seen by Maute et al. (2015) and J. C. Wang et al. (2017) for other SSW events. By contrast, the 4D Tend simulation has a much broader region of strong eastward equatorial winds without the sharp jump at the nudging boundary.

To better understand the origins of these steep vertical gradients in the simulated mean zonal winds in the SD_{zm} and SD_{full} cases and not in the 4D Tend case, Figure 5 illustrates the zonal and daily mean zonal wind

tendencies at the equator for 27 January and 9 February 2010. Shown are the SD_{zm} (Figures 5b and 5f), SD_{full} (Figures 5c and 5g), and 4D Tend (Figures 5d and 5h) cases, as well as the purely ECMWF + GSWM-driven simulation (first column). In the purely driven case, mean zonal wind tendencies remain small up to $\sim 5 \times 10^{-4}$ hPa, above which GWD (green line), vertical advection (red line), and vertical viscosity (orange line) grow in magnitude and determine the zonal mean zonal wind structure. More importantly in this case all equatorial zonal wind tendencies shown in Figures 5a and 5e vary smoothly with altitude, especially in the MLT region. However, in the SD_{zm} and SD_{full} cases, GWD, vertical advection, and vertical viscosity tendency terms all exhibit significant increases in the altitude regime surrounding the nudging boundary. For example, strong eastward acceleration (on the order of $200 \text{ m} \cdot \text{s}^{-1} \cdot \text{day}^{-1}$) in the zonal mean zonal winds due to GWD is calculated in January and February for the SD_{zm} and SD_{full} cases, consistent with findings of Maute et al. (2015) and J. C. Wang et al. (2017). The TIME-GCM appears to try and balance this strong eastward GWD force induced by the SD_{zm} and SD_{full} nudging schemes, through vertical advection and viscosity (see red and orange lines in Figures 5b and 5c and Figures 5f and 5g).

Figures 5d and 5h illustrate why 4D Tend zonal mean zonal winds vary smoothly across the nudging boundary. Similar to the zonal mean zonal wind tendencies shown in Figures 5a and 5e for the TIME-GCM ECMWF + GSWM (driven) case, zonal mean zonal wind tendencies in the 4D Tend case vary smoothly with height through the vertical domain of the TIME-GCM. (Note the westward acceleration of $\sim 50 \text{ m} \cdot \text{s}^{-1} \cdot \text{day}^{-1}$ seen near 1 hPa in Figures 5d and 5h is introduced in the TIME-GCM to account for the semiannual oscillation in tropical zonal wind near 1 hPa; e.g., Smith, Garcia, et al., 2017, that is present in NAVGEM-HA but not in the TIME-GCM ECMWF + GSWM; see Figure S3 in the supporting information for more details on this feature). Near ~ 90 km, the 4D Tend case shows moderate eastward GWD ($\sim 75 \text{ m} \cdot \text{s}^{-1} \cdot \text{day}^{-1}$), which is not present in the purely driven simulation. This smoothly varying moderate GWD drag is in balance with the artificial tendency term calculated in the 4D Tendency nudging scheme (purple line Figures 5d and 5h). Also note that no other mean zonal wind tendency terms in the 4D Tend case drastically change in response to nudging the dynamical fields.

This is a key characteristic of 4D Tendency nudging, which appears to isolate the essential differences between the driven TIME-GCM and NAVGEM-HA simulations as at least partially due to differences in gravity wave forcing or propagation (especially in the tropics at MLT altitudes). In this way, the artificial tendency term attempts to force the equatorial mean zonal winds away from their climatological state toward NAVGEM-HA (i.e., Figure 4a), which is then compensated for by increased GWD back toward their TIME-GCM driven state (i.e., Figure 4b). Note that differences in resolved-scale wave forcing, in addition to small-scale GWD, may also contribute to the zonal mean zonal wind differences between the NAVGEM-HA and TIME-GCM-driven simulations, and thus the nudging term. As a result, the parameterized GWD term in TIME-GCM most strongly responds to this nudging term because zonal momentum balance in the MLT region depends on GWD (e.g., Liu et al., 2009). Conversely, where TIME-GCM-driven-NAVGEM-HA differences are small, parameterized model forcings are consistent with their TIME-GCM-driven values.

Figures 4 and 5 demonstrate that 4D Tendency nudging allows one to place a direct constraint on the dynamical fields in the TIME-GCM and not induce zonal mean artifacts attributable to differences between TIME-GCM and NAVGEM-HA and their parameterization schemes. Since the driven TIME-GCM simulation does not reproduce the overall zonal mean zonal wind structure simulated by NAVGEM-HA in Figure 4, our subsequent analysis focuses on only the nudged TIME-GCM simulations. Further, since the model dynamical and parameterized quantities in the 4D Tend simulation appear to be in balance, while the model dynamical and parameterized quantities in the SD_{zm} and SD_{full} simulations do not, thus, we subsequently quantify the effects of these differences on the mean MLT and TI and investigate what causes these differences among the different nudging techniques.

Figure 6 shows the zonal mean meridional (a–c) and vertical (d–f) winds from our SD_{zm} , SD_{full} , and 4D Tend simulations averaged from 1 January to 21 March 2010. Analogous to the average zonal mean zonal winds, the zonal mean meridional winds in the SD_{zm} and SD_{full} simulations exhibit a strong increase at pressure levels immediately above the nudging boundary. Northward winds at tropical southern latitudes reach up to 20 m/s, while southward winds at tropical northern latitudes reach -8 m/s in the SD_{zm} and SD_{full} simulations (Figures 6a and 6b). Force term analysis of the zonal mean meridional momentum equation indicates that these strong vertical gradients are driven by sharp increases in the Coriolis (in response to the strong vertical gradients in the average zonal winds, Figure 4), pressure gradient, and vertical viscous forces at the nudging boundary (see Figure S4). This average convergence of meridional winds over the equator, coupled with the

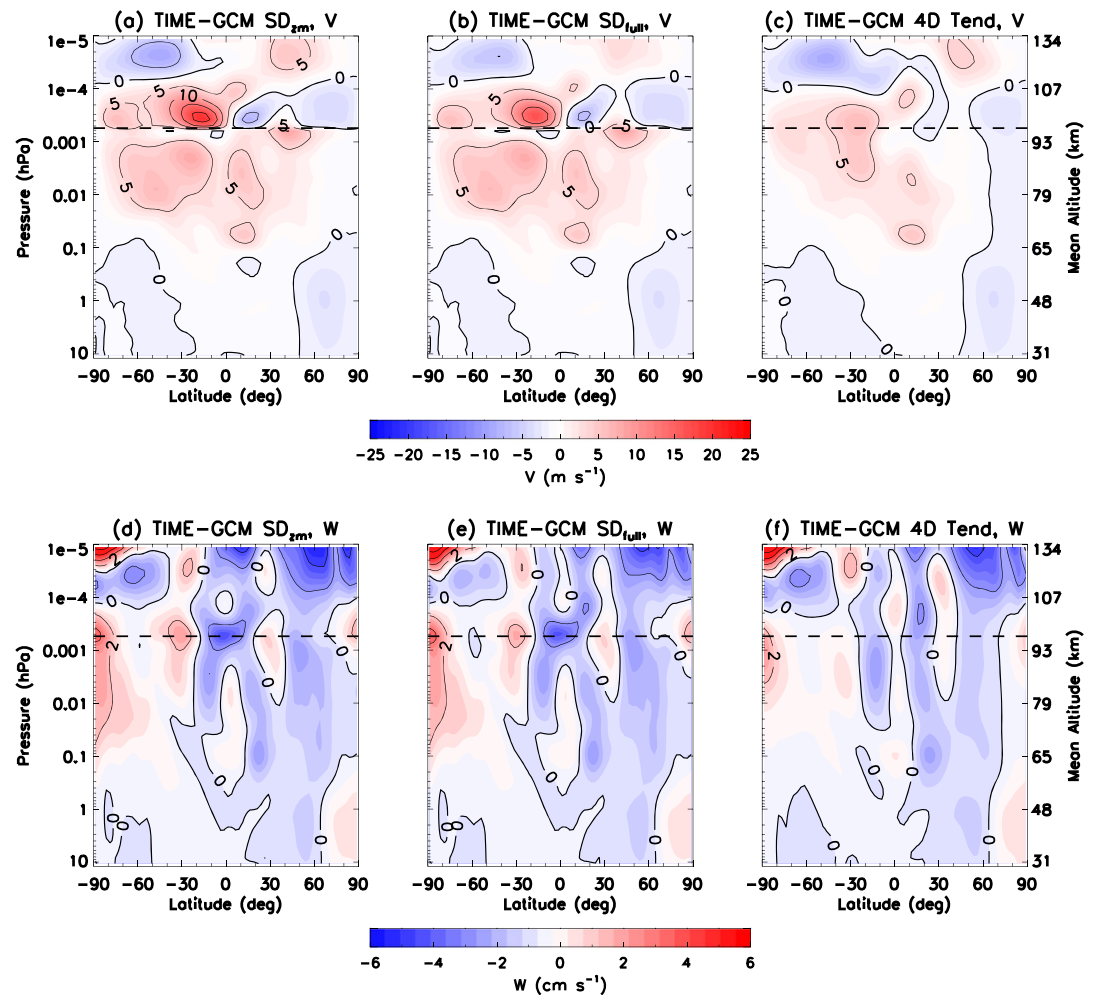


Figure 6. Zonal mean meridional (a–c) and vertical (d–f) winds averaged from 1 January to 21 March 2010 as a function of latitude and pressure/mean altitude simulated by TIME-GCM SD_{zm} (a and d), SD_{full} (b and e), and 4D Tend (c and f). Meridional (Vertical) winds are contoured every ± 5 m/s (± 2 cm/s). The bold dashed line indicates where $\zeta = 0$, below (above) which the TIME-GCM is constrained (free running) in the different nudging simulations. TIME-GCM = thermosphere-ionosphere-mesosphere-electrodynamics general circulation model; SD = specified dynamics.

strong eastward winds depicted in Figure 4, produces comparatively strong downwelling in the SD_{zm} and SD_{full} simulations, with average vertical winds of -3 cm/s during the boreal winter months (Figures 6d and 6e). In the 4D Tend case, average meridional winds evolve smoothly with altitude across the nudging boundary, with weaker wind speeds (i.e., reaching up to ~ 8 m/s at low latitudes; Figure 6c). Consequently, weaker convergence/divergence of average zonal and meridional winds leads to weaker vertical winds in Figure 6f at equatorial latitudes in the MLT region. Since the zonal mean meridional circulation in the MLT region can have profound effects on TI composition (e.g., Jones, Forbes, Hagan, & Maute, 2014; Liu & Roble, 2002; Yamazaki & Richmond, 2013), this implies that the differences shown here may have consequences on the calculated compositional morphology of the TI system. This is discussed further in section 3.4.

3.3. Atmospheric Tides and Planetary Waves

The 2010 SSW event was driven by the rapid intensification of planetary wave 1 (PW1) at 10 hPa in middle/late January (see Figure 7 and ; Goncharenko et al., 2013), the effects of which were observed in the middle and upper atmosphere several weeks after the initial planetary wave intensification. Given the documented role planetary waves and tides play in coupling day-to-day lower and middle atmospheric variability to short-term TI variability (e.g., Chang et al., 2009; Chau et al., 2011; Funke et al., 2010; Pedatella & Forbes, 2010; Pedatella & Liu, 2013; Yamazaki et al., 2015), it is important to understand how SD and 4D Tendency nudging differentially affect the vertical wave spectrum in light of the results presented in section 3.2. Note that we only show the

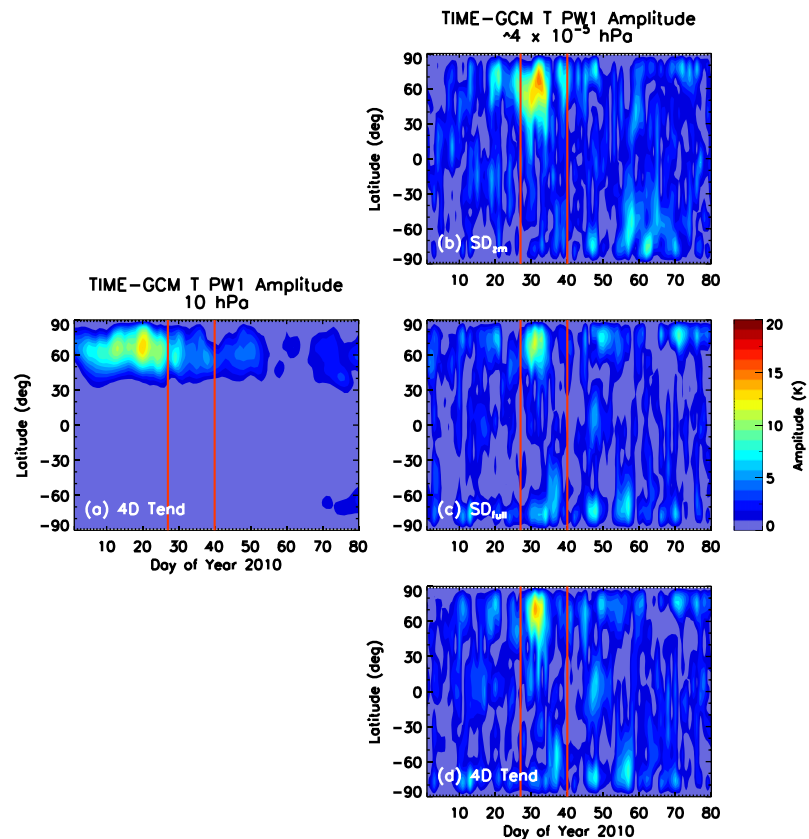


Figure 7. PW1 temperature amplitude at 10 hPa (~ 30 km) from the 4D Tend TIME-GCM simulation (4D Tend, a), as a function of day of year in 2010 and latitude. (b–d) Same as Figure 7a except at 3.96×10^{-5} hPa (~ 115 km) from the SD_{zm} (b), SD_{full} (c), and 4D Tend (d) TIME-GCM simulations. The red vertical lines at 27 January and 9 February 2010 denote the two different onset criteria for sudden stratospheric warmings, see Figure 1 and surrounding text for details. TIME-GCM = thermosphere-ionosphere-mesosphere-electrodynamics general circulation model; SD = specified dynamics.

amplitudes of individual wave components, as simulated phases in the SD_{zm}, SD_{full}, and 4D Tend cases were not drastically different (i.e., within a couple of hours of one another).

Figure 7 shows the variability of PW1 temperature amplitudes at both 10 hPa (~ 30 km) and 3.96×10^{-5} hPa (~ 115 km). The simulated temporal variability of PW1 temperature amplitudes at 10 hPa and 3.96×10^{-5} hPa in all the simulations are similar, with only minor (~ 2 – 4 K) absolute amplitude differences between the SD_{zm}, SD_{full}, and 4D Tend cases. (i.e., SD_{zm} and SD_{full} PW1 amplitudes at 10 hPa are shown in Figure S5 in the supporting information). The 4D Tend TIME-GCM simulations illustrate that PW1 reached its maximum amplitude on day 19, with amplitudes of ~ 15 K. A secondary enhancement beginning on day 29 at 10 hPa is also evident in the 4D Tend simulation, with maximum PW1 amplitudes approximately a third of those reported on day 19.

In contrast to the stratosphere, all the model simulations show that at lower thermospheric altitudes (i.e., 3.96×10^{-5} hPa), the initial enhancement of PW1 at day 19 is significantly weaker than the enhancement beginning on day 29. In the lower thermosphere, PW1 temperature amplitudes from SD_{zm} and 4D Tend more closely correspond, reaching maximum amplitudes of 17 and 16 K in late January/early February, while SD_{full} shows a peak PW1 temperature amplitude of 13 K at high northern latitudes. The initial PW1 enhancement around day 19 in the SD_{zm} case is also larger than in the SD_{full} and 4D Tend simulations. Small differences also occur around day 50 at low latitudes between the SD_{zm}, SD_{full}, and 4D Tend cases. In general, there is overall agreement in the simulated PW1 using different nudging techniques, with only minor differences at stratospheric and lower thermospheric altitudes.

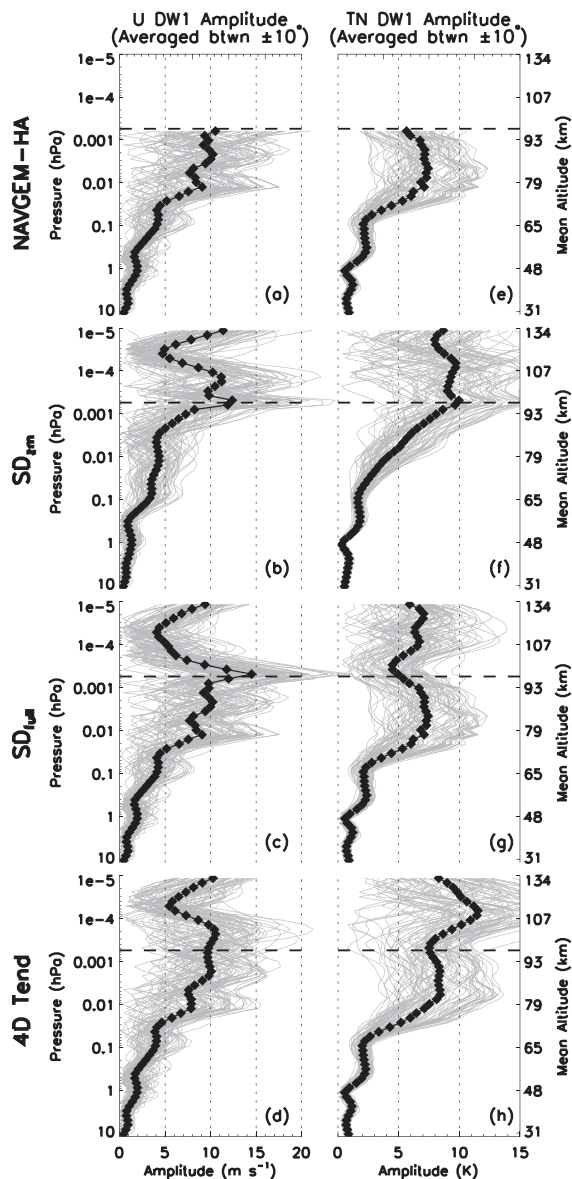


Figure 8. Vertical profiles of the DW1 daily (gray) and mean (black diamonds) zonal wind amplitude averaged between $\pm 10^\circ$ latitude from 1 January to 21 March 2010 from (a) NAVGEM-HA, TIME-GCM SD_{zm} (b), TIME-GCM SD_{full} (c), and TIME-GCM 4D Tend (d). (e–h) Same as Figures 8a–8d except for DW1 temperature amplitudes. The bold dashed line indicates where $\zeta = 0$, below (above) which the TIME-GCM is constrained (free running) in the different nudging simulations. TIME-GCM = thermosphere-ionosphere-mesosphere-electrodynamics general circulation model; NAVGEM-HA = Navy Global Environmental Model a high-altitude version; SD = specified dynamics.

Figure 8 shows the migrating (i.e., westward propagating) diurnal tide with zonal wave number 1 (DW1) zonal wind (a–d) and temperature (e–h) amplitude variability averaged over equatorial latitudes (i.e., $\pm 10^\circ$) from NAVGEM-HA and our TIME-GCM simulations. In general, considering first the zonal winds, the vertical variation of DW1 in the 4D Tend case is smoother than in either SD_{zm} or SD_{full} where discontinuities are seen at the nudging boundary. This sharp increase in DW1 zonal wind amplitudes is a by-product of the sharp vertical gradients in the zonal mean zonal winds depicted in Figure 4. Vertical profiles of DW1 mean and daily zonal wind amplitudes from 4D Tend track NAVGEM-HA and smoothly transition across the nudging boundary with a mean amplitude of 10 m/s. There are also subtler differences between the three cases; for example, the amplitude of DW1 in the SD_{zm} case in the upper mesosphere (~ 0.01 hPa) is considerably smaller (near 5 m/s) than in either the other two cases or in NAVGEM-HA. In general, the SD_{full} case comes closest to matching NAVGEM-HA, which is not surprising since both zonal mean and wave fields are tightly coupled to NAVGEM-HA. However, unlike 4D Tend, it suffers from the aforementioned sharp discontinuity when nudging stops. Above ~ 96 km, simulated DW1 zonal wind amplitudes decrease up to ~ 107 km and then increase again reaching ~ 10 m/s due to in situ absorption of extreme ultraviolet radiation by O_2 .

The simulated DW1 temperature amplitudes from SD_{full} do not exhibit sharp vertical gradients surrounding the nudging boundary. Specifically, the SD_{full} DW1 temperature amplitudes ranging from 5 to 10 K follow the NAVGEM-HA DW1 temperature amplitudes below ~ 96 km, peaking at ~ 80 km. Above ~ 80 km, DW1 temperature amplitudes decrease in the SD_{full} to ~ 5 K at ~ 100 km and increase slightly back to ~ 7 K by ~ 130 km, with daily amplitude variations on the order of 10 K or more. The 4D Tend DW1 temperature amplitudes are similar to those simulated in the SD_{full} case, except that they tend to be 3–5 K greater in magnitude, and there is a clear secondary average amplitude peak of ~ 12 K at ~ 107 km. Zhang et al. (2010a, 2010b) observed this two-peak DW1 vertical amplitude structure in monthly mean March TIMED Sounding of the Atmosphere using Broadband Emission Radiometry (SABER) observations, with the first amplitude peak occurring at 80–85 km and the second at 95–100 km. Furthermore, Akmaev et al. (2008) showed mean January–March DW1 temperature amplitudes at low latitudes from SABER ranging from 10 to 18 K at 100 km, which 4D Tend appears to reproduce. It is interesting that this two-peak DW1 vertical structure is only seen in the SD_{full} and 4D Tend cases, and not in the SD_{zm} case. This may reflect the fact that the SD_{full} and 4D Tend cases apply constraints to both zonal mean and wavefields, whereas the SD_{zm} case only constrains the zonal mean temperature fields, and not the wavefields. The SD_{zm} field seems to continue increasing above the ~ 96 -km nudging boundary and produces large daily variations in DW1 amplitudes (similar to the 4D Tend case). In general, it is not immediately evident why the three cases differ in simulating DW1; however, it is clear that different

nudging techniques can lead to different tidal behavior up into the lower thermosphere. As we will show below, these difference can have important ionospheric consequences.

Other atmospheric tidal components including the migrating (i.e., westward propagating) semidiurnal tide with zonal wave number 2 (SW2) and the westward propagating nonmigrating semidiurnal tide with zonal wave number 1 (SW1) are known to appreciably influence the ionospheric electrodynamics of the E region during SSWs (e.g., Fang et al., 2012; Lin et al., 2013; Liu et al., 2010; Pedatella, Richmond, et al., 2016, and references therein). Thus, for ionospheric applications, it is important to understand how different nudging techniques affect the SW2 and SW1 during the 2010 SSW. Figure 9 shows the SW2 (a–c) and SW1 (d–f)

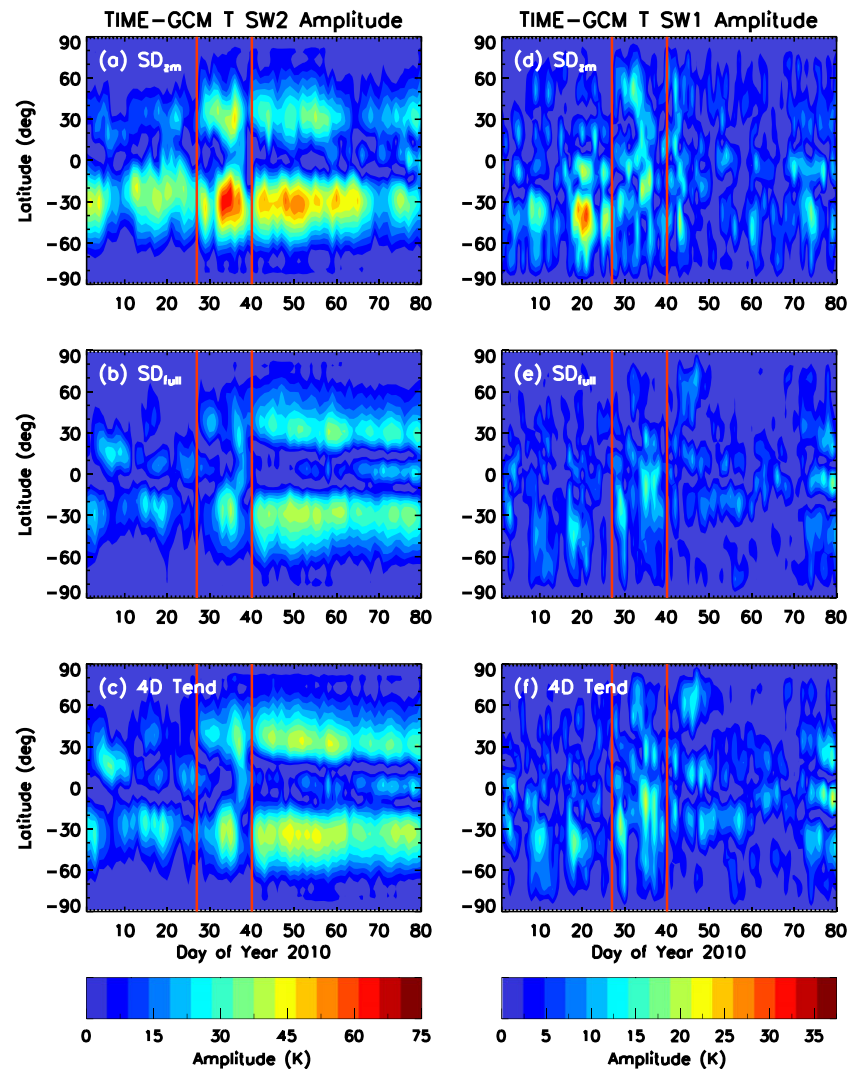


Figure 9. SW2 temperature amplitude at 3.96×10^{-5} hPa (~ 115 km) from SD_{zm} (a), SD_{full} (b), and 4D Tend (c) TIME-GCM simulations as a function of day of year in 2010 and latitude. (d–f) Same as Figures 9a–9c except for SW1. The red vertical lines at 27 January and 9 February 2010 denote the two different onset criteria for sudden stratospheric warmings; see Figure 1 and surrounding text for details.

temperature amplitudes at 3.96×10^{-5} hPa (~ 115 km). Overall, the SD_{full} and 4D Tend amplitudes in Figure 9 are comparable for all the tides depicted, with SD_{zm} showing larger maximum amplitudes for SW2 and SW1. Specifically, SW2 maximum amplitudes of 73 K occur between days 30 and 37 in the SD_{zm} simulation, whereas maximum amplitudes of 53 and 49 K occur between days 50 and 55 (well after the SSW) in the 4D Tend and SD_{full} simulations, respectively.

The differences between the SD_{zm} simulated SW2 and SD_{full} /4D Tend simulated SW2 probably arise due to different methods of constraint for the wave perturbations in the model. For example, SW2 is mainly driven by ozone absorption in the stratosphere, and SD_{full} and 4D Tend constrain the full temperature field (i.e., zonal mean plus wave perturbations) throughout the stratosphere and mesosphere, so as to project the ozone variability from NAVGEM-HA onto TIME-GCM temperature fields. In the SD_{zm} simulation, only the zonal mean temperature field is constrained by NAVGEM-HA above the TIME-GCM lower boundary so that the internal ozone variability simulated in the TIME-GCM drives the SW2 calculated in Figure 9a. Similar to what Goncharenko et al. (2012) concluded for the 2009 SSW, Figures 9a–9c suggest that ozone variability during SSWs may be important for driving SW2 differences in the MLT region.

Figures 9d–9f also show similar spatiotemporal variability simulated for the SW1 in our three different TIME-GCM simulations. Stronger SW1 amplitudes are calculated in the SD_{zm} simulation. This is a consequence of stronger SW2 amplitudes simulated in the SD_{zm} case, as SW1 is mainly generated through nonlinear interaction between PW1 and SW2 (Liu et al., 2010). Slight amplitude differences occur in other nonmigrating tidal components as well (e.g., the eastward propagating diurnal tide with zonal wave number 2, not shown) as a result of different methods of constrain applied to both the waves themselves, in addition to the dynamics that determine wave propagation characteristics. In summary, the vertical, temporal, and spatial variability of the simulated planetary waves and tides during the 2010 boreal winter months are moderately affected by different nudging methods, with the largest differences calculated for the migrating tides. Better agreement between all the nudging experiments for the nonmigrating tidal components is important because these waves are responsible for driving the longitudinal variability observed in the F region ionosphere (e.g., Pedatella & Liu, 2013).

3.4. Implications for Neutral Composition and the Ionosphere

As noted earlier, neutral dynamics in the MLT region can have important effects on thermospheric atomic oxygen (O). Subsequently, these effects can propagate up to higher altitudes and impact the ionosphere (e.g., Jones, Forbes, & Hagan, 2014; Jones, Forbes, Hagan, & Maute, 2014; Pedatella, Richmond, et al., 2016; Siskind et al., 2014; Yamazaki & Richmond, 2013). Given the previously presented zonal mean and tidal results, analyzing the effects SD and 4D Tendency nudging have on the simulated variability of O in the mesosphere and thermosphere, as well as electron densities in the F region ionosphere, is warranted.

Figures 10a and 10b illustrate the effects of different nudging approaches on the simulated mean O number density ($[O]$) at low and middle latitudes over the period of study. Above ~ 85 km, SD_{zm} (blue), SD_{full} (green), and 4D Tend (red) TIME-GCM simulated average $[O]$ values are different, with 4D Tend $[O]$ being larger than SD_{zm} and SD_{full} . Specifically, O peak densities of $\sim 4 \times 10^{11} \text{ cm}^{-3}$ are simulated in the 4D Tend case, while SD_{zm} and SD_{full} O peak densities are $\sim 2\text{--}3 \times 10^{11} \text{ cm}^{-3}$ (or $\sim 40\%$ lower, Figure 10b). Figure 10a also reveals that the peak $[O]$ simulated by TIME-GCM is sensitive to the nudging technique employed to constrain the model dynamics. Even though all simulated peak $[O]$ values are low compared to the NRL Mass Spectrometer Incoherent Scatter (NRLMSISE00) empirical model values (Picone et al., 2002), discrepancies between modeled and NRLMSISE00 peak $[O]$ grow from $\sim 30\%$ in the 4D Tend case to $\sim 50\%$ in the SD_{zm} and SD_{full} cases. Above the $[O]$ peak, molecular diffusion time scales become very rapid, and each simulated $[O]$ profile decreases following its own scale height via the barometric law. As a result, 4D Tend simulated $[O]$ remains approximately $\sim 10\text{--}30\%$ higher than SD_{zm} and SD_{full} simulated $[O]$ (Figure 10b; note that the small-scale oscillations in the percent difference vertical profiles are numerical artifacts of interpolation from log pressure to height coordinates). But these 4D Tend simulated $[O]$ values are still lower than NRLMSISE00 $[O]$ values by $\sim 25\%$ at 300 km, suggesting that TIME-GCM simulated ionospheric densities will also be lower than expected.

The cause of the differences in modeled O abundances is likely the differences in mean meridional circulation and tidal transport at the nudging boundary (i.e., near the peak in O concentration). In turn, these differences arise from some of the discontinuities seen in the SD_{zm} and SD_{full} cases that are relatively absent in the 4D Tend simulation. Thus, in the SD_{zm} and SD_{full} simulations, strong eastward mean zonal winds (Figure 4) surrounding the nudging boundary are balanced by strong meridional wind convergence and downward vertical winds (Figure 6). Additionally, the spikes in DW1 amplitudes seen at the nudging boundary in the SD_{zm} and SD_{full} cases likely also contribute to enhanced downward transport (compared to 4D Tend, Figure 8). The aggregate affect is lower $[O]$ values in the SD_{zm} and SD_{full} simulations due to nudging-induced increased zonal mean meridional/vertical and DW1 tidal transport, as more O is transported downward into the mesosphere and subsequently lost via recombination (see Forbes et al., 1993). This is consistent with earlier studies of these effects on $[O]$ in the NCAR thermosphere GCMs (e.g., Jones, Forbes, & Hagan, 2014; Yamazaki & Richmond, 2013).

Figures 10c–10e show that these systematic differences in MLT $[O]$ are linked to important differences in calculated ionospheric electron densities. These figures show the daytime (i.e., $12 \text{ LT} \pm 1.5 \text{ hr}$ in local time) median peak electron densities in the F region ($N_m F_2$) ionosphere as a function of day of year and magnetic latitude. Figure 10f is analogous to Figures 10c–10e, except measured by the COSMIC satellites (e.g., Anthes et al., 2008). The COSMIC profiles were obtained from the COSMIC Data Acquisition and Analysis Center (<http://cdaac-www.cosmic.ucar.edu/cdaac/>). Processing for the median daytime (nighttime in the supporting information) $N_m F_2$ follows that of Burns et al. (2012), except that a 10-day running median was applied instead

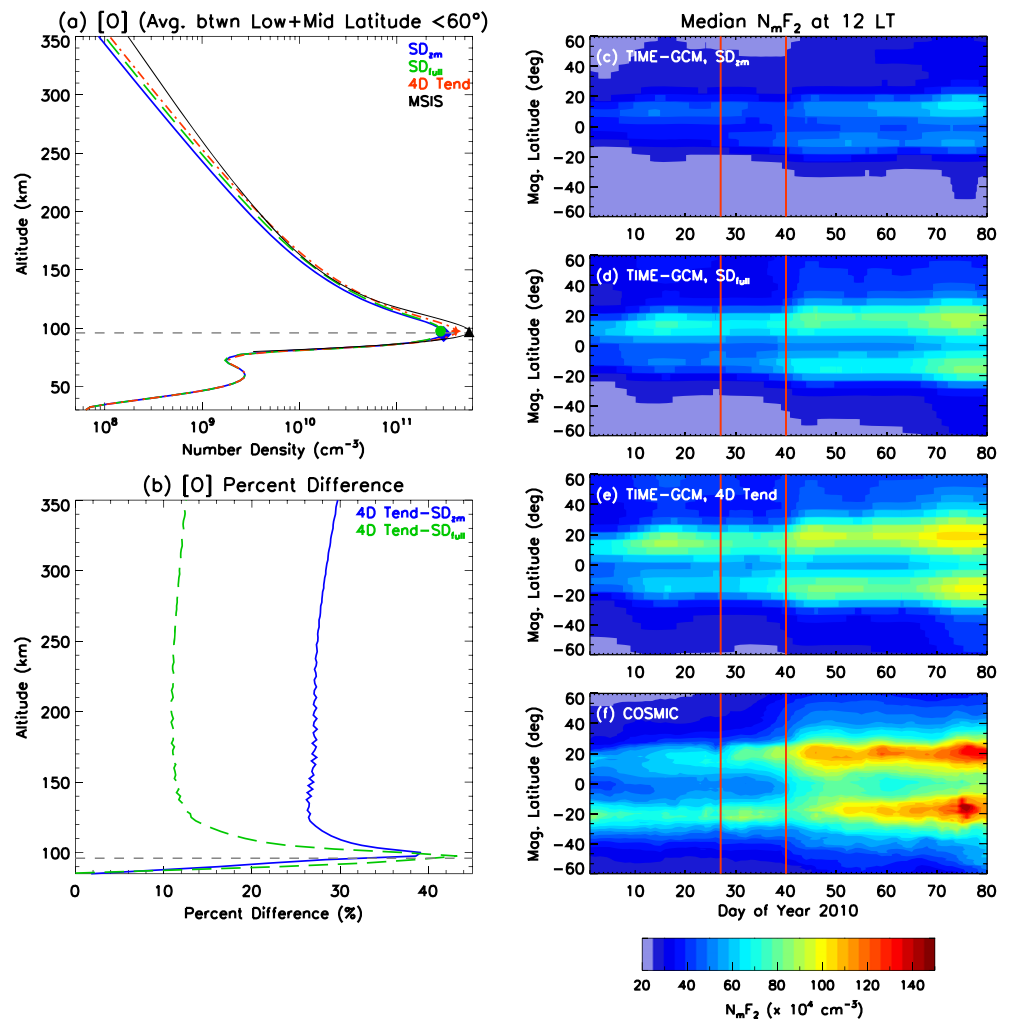


Figure 10. (a) Vertical profile of [O] averaged from 1 January to 21 March 2010 and over geographic low and middle latitudes (i.e., $\pm 60^\circ$) from SD_{zm} (blue), SD_{full} (green), 4D Tend (red) TIME-GCM simulations, and NRLMSISE00 (black). (b) [O] percent differences between 4D Tend and SD_{zm} (SD_{full}) TIME-GCM simulations depicted in (a) above 85 km. Median local noon (12 LT ± 1.5 hr in local time) $N_m F_2$ values from SD_{zm} (c), SD_{full} (d), 4D Tend (e) TIME-GCM simulations, and (f) COSMIC observations as a function day of year in 2010 and magnetic latitude. The gray bold dashed line in (a) and (b) indicates where $\zeta = 0$, below (above) which the TIME-GCM is constrained (free running) in the different nudging simulations. The red vertical lines at 27 January and 9 February 2010 denote the two different onset criteria for sudden stratospheric warmings; see Figure 1 and surrounding text for details. The different symbols in (a) mark the maximum [O] value in the different TIME-GCM simulations. TIME-GCM = thermosphere-ionosphere-mesosphere-electrodynamics general circulation model; SD = specified dynamics; COSMIC = Constellation Observing System for Meteorology, Ionosphere, and Climate.

of a 30-day running median, with a running 10° bin in latitude, for all COSMIC observations between 1030 to 1330 solar local time. Note that the TIME-GCM simulated median daytime (and nighttime) $N_m F_2$ results are processed following the same technique as the COSMIC observations, except that all the grid points within the same binning interval are included.

Both the SD and 4D Tendency nudging approaches reproduce the spatiotemporal variability associated with the noontime median $N_m F_2$ observed by COSMIC, including the 2010 SSW period (Figures 10c–10f). However, the direct impact of increased mixing and decreased [O] in the SD_{zm} and SD_{full} cases results in low median daytime and nighttime (see Figure S6 in the supporting information) $N_m F_2$ values, compared to COSMIC. For example, SD_{zm} and SD_{full} simulated maximum median $N_m F_2$ values never exceed $1.0 \times 10^6 \text{ cm}^{-3}$, whereas COSMIC observed maximum median $N_m F_2$ exceed $1.5 \times 10^6 \text{ cm}^{-3}$ approaching vernal equinox in the equatorial ionization anomaly crests. Although 4D Tend simulated median $N_m F_2$ values are larger than those simulated

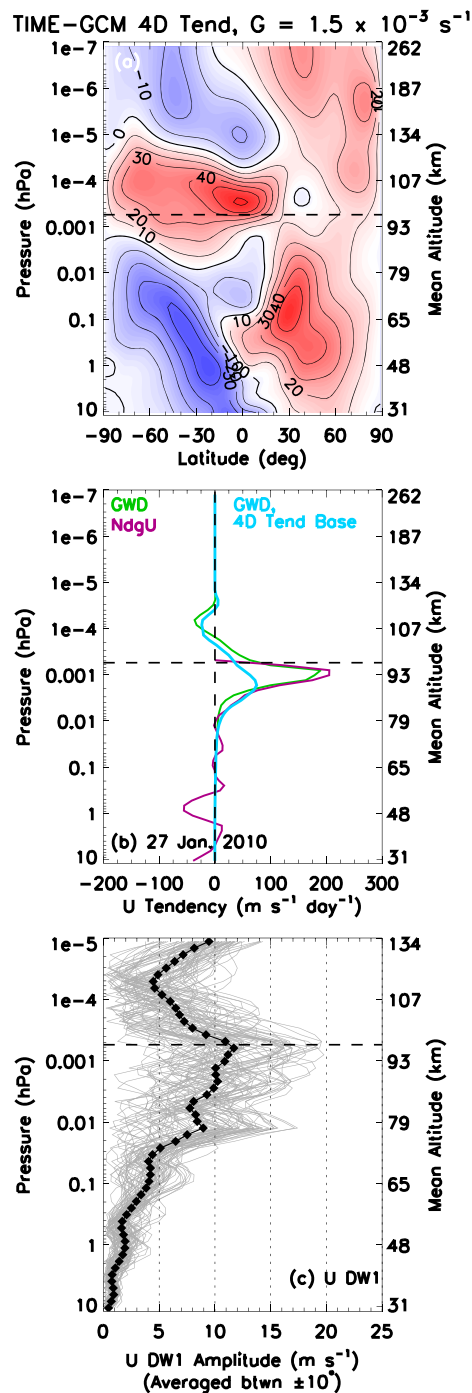


Figure 11. (a–c) Same as Figures 4e, 5d, and 8d, respectively, except using a G of $1.5 \times 10^{-3} \text{ s}^{-1}$ or *strong G*. (a) Shown are the zonal mean zonal winds averaged from 1 January to 21 March 2010. (b) Daily averaged zonal mean zonal wind tendencies at the equator on 27 January 2010. (c) Vertical profiles of the DW1 daily (gray) and mean (black diamonds) zonal wind amplitude averaged between $\pm 10^\circ$ from 1 January to 21 March 2010. The wind tendencies depicted in Figure 11b are GWD (green), the artificial nudging tendency term (NdgU, purple), and GWD from the 4D Tend TIME-GCM simulation with a *weak G* of $1.5 \times 10^{-4} \text{ s}^{-1}$ or *4D Tend Base Case* (GWD, cyan). The bold dashed line indicates where $\zeta = 0$, below (above) which the TIME-GCM is constrained (free running). TIME-GCM = thermosphere-ionosphere-mesosphere-electrodynamics general circulation model; GWD = gravity wave drag.

by SD_{zm} and SD_{full} , they are still ~ 10 – 30% too low compared to COSMIC observations. Midnight median $N_m F_2$ from the SD_{zm} , SD_{full} , and 4D Tend TIME-GCM simulations are also too low compared to COSMIC (Figure S6). Since the zonal mean wind circulation and tidal perturbations in our 4D Tend simulation do not exhibit nudging artifacts around the nudging boundary (and thus less vigorous downward transport), low median $N_m F_2$ values suggest that [O] is still too low and that further reducing TIME-GCM K_{zz} near the mesopause (i.e., already reduced by a factor of 10) may be warranted. Additional examination of these simulated low MLT O values in TIME-GCM deserves future consideration, especially given the interplay between dynamics and chemistry at MLT altitudes.

4. Discussion

4.1. Sensitivity to Relaxation Factor

As briefly discussed in section 2.4, the 4D Tendency nudging method described herein requires a user-specified, and somewhat arbitrary relaxation factor G [s^{-1}]. Based on numerical weather prediction results in the troposphere and stratosphere, Stauffer and Seaman (1990), Zou et al. (1992), and Jeuken et al. (1996) discussed the importance of choosing the proper G . Specifically, Stauffer and Seaman (1990) recommend selecting G to be similar to the slowest physical adjustment process in the model of interest, as model fields will approach the observed fields with an e -folding time of $1/G$ (i.e., the relaxation time in seconds). When trying to constrain dynamical fields spanning the ~ 30 – $1,000$ -km altitude regime, selecting the proper G can be difficult because the slowest processes vary regularly with height. Applying a stronger G retains higher-frequency fluctuations (i.e., wave perturbations important for simulating SSWs, for example) but the observed variability will dominate the model forcing. Recently, Song et al. (2018) utilized a whole atmospheric model to compute the modeled GWD forcing in the MLT region (and resulting residual mean circulation) as a function of the relaxation factor (or what they refer to as the nudging time scale). They found that for dynamically initializing their whole atmosphere model the optimal relaxation factor was between 4 and 48 hr. For our baseline example, however, we chose G in our 4D Tend TIME-GCM simulations to be the same as Siskind and Drob (2014) and Siskind et al. (2014) used in their TIE-GCM experiments (i.e., $1.5 \times 10^{-4} \text{ s}^{-1}$ or ~ 1.85 hr), but the practical effects of selecting this value have remained unexamined. To examine the sensitivity of our results to changing G , we performed two additional simulations where G was increased by factors of ~ 5 and 10.

Figure 11 illustrates the effects that increasing G in the 4D Tendency nudging scheme can have on the zonal mean zonal winds and DW1 zonal wind amplitudes. Specifically, Figures 11a–11c are from TIME-GCM simulations that increased G by a factor of 10 from what is shown in Table 1 to $1.5 \times 10^{-3} \text{ s}^{-1}$ (or *strong G*). The most noticeable differences occur surrounding the nudging boundary (bold dashed line), as stronger coupling to NAVGEM-HA zonal winds generate a stronger vertical gradient in the low-latitude mean zonal winds. Equatorial mean zonal wind tendency terms calculated on 27 January 2010 indicate that this stronger vertical gradient and stronger eastward winds just above the nudging boundary result from increased eastward GWD between 0.01 and $5.5 \times 10^{-4} \text{ hPa}$ (green line, Figure 11b). Compared to the *4D Tend Base Case* (i.e., the 4D Tend simulations described in Table 1 with a G of $1.5 \times 10^{-4} \text{ s}^{-1}$, or *weak G*), GWD tendencies have increased in this region by a factor of ~ 3 from

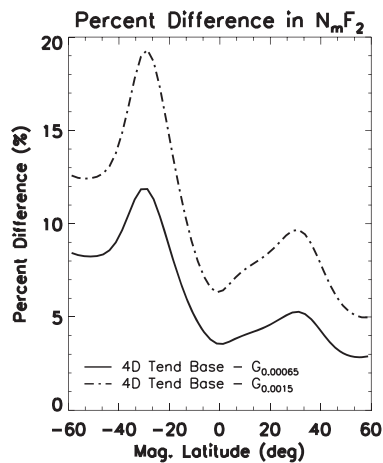


Figure 12. Percent differences in the zonal mean $N_m F_2$ averaged between day of year 40 and 80 in 2010 as a function of magnetic latitude. Shown in solid (dashed dot) line is the percent difference from the 4D Tend Base Case with $G = 1.5 \times 10^{-4} \text{ s}^{-1}$ or weak G case relative to the 4D Tend $G = 6.5 \times 10^{-4} \text{ s}^{-1}$ ($G = 1.5 \times 10^{-3} \text{ s}^{-1}$) or medium G (strong G) case.

the supporting information.) By increasing G , Figure 11 shows that one can better reproduce the observed dynamics in the MLT region. Since NAVGEM-HA winds and tides compare well to observations during the 2010 SSW event (McCormack et al., 2017), increasing G to even higher values may be desired for a study focused on MLT region dynamics. However, increasing G could have adverse side effects for those interested in understanding ionospheric variability, as indicated by the results presented in sections 3.2–3.4.

Figure 12 illustrates the effects that increasing G in the 4D Tendency nudging scheme can have on the electron density of the F region ionosphere. Depicted is the percent difference in the zonal mean $N_m F_2$ averaged from the onset of the major SSW event (day of year 40) to the March equinox (day of year 80) from the 4D Tend Base Case with weak G , relative to the 4D Tend cases with medium (solid line) and strong (dashed dot) G . Increasing G in TIME-GCM results in smaller average $N_m F_2$ after SSW onset (i.e., positive percent differences in Figure 12 represent greater $N_m F_2$ in the 4D Tend Base Case or weak G case compared to the medium and strong G cases). Increasing G by a factor of ~ 5 (10) results in a ~ 5 – 10% (~ 10 – 20%) decrease in electron density in the F_2 region ionosphere, making $N_m F_2$ that are already too low relative to COSMIC (see Figure 10) even lower. Decreased $N_m F_2$ values result from increased nudging-induced downward transport via increased zonal mean winds and tidal amplitudes in the MLT region (as indicated by the results presented in Figure 11). Recall that eddy diffusion (K_{zz}) values in our nudged TIME-GCM simulations herein already reduced by a factor of 10 from their nominal values, but results presented in Figure 12 suggest that K_{zz} could be reduced even further as G increases (similar to what ; Siskind et al., 2014, found by including nonmigrating tides at the TIE-GCM lower boundary). Also, the largest differences in $N_m F_2$ are located in the southern equatorial ionization anomaly crest, the explanation for which warrants further investigation, but is most likely model specific, and therefore is beyond the scope of this investigation.

4.2. Connecting SD and 4D Tendency Nudging

Here we show, based upon the results of the previous section, that although SD and 4D Tendency nudging are conceptually different, the apparent differing outcomes can be reconciled. This is because both approaches are ultimately forms of Newtonian relaxation.

In 4D Tendency nudging the model relaxation time is calculated as the inverse of the relaxation factor, $1/G$. For our 4D Tend simulation described in Table 1, a G of $1.5 \times 10^{-4} \text{ s}^{-1}$ corresponds to a relaxation time of ~ 1.85 hr. In SD nudging, model relaxation time is determined by the product of the small parameter α and the model time step Δt . SD_{zm} and SD_{full} simulations assumed $\alpha = 1$, and all of the simulations performed herein used a Δt of 30 s, meaning that SD_{zm} and SD_{full} simulations had a model relaxation time of 30 s (or 8.33×10^{-3} hr). However, the developments described by Stauffer and Seaman (1990) suggest that a model relaxation time as strong as this would not allow TIME-GCM model physics time to adjust (or relax) toward the data set used for nudging.

~ 75 to $\sim 200 \text{ m} \cdot \text{s}^{-1} \cdot \text{day}^{-1}$. As expected, increased G results in a stronger artificial tendency term (via equation (4)), which is then compensated for by increased GWD close to the nudging boundary. Although not depicted in Figure 11, horizontal and vertical advection terms, as well as vertical viscous forces, increase close to the nudging boundary in response to changes in the other tendency terms when G is increased.

Low-latitude DW1 zonal wind amplitudes shown in Figure 11c increase at the nudging boundary in response to strong eastward equatorial zonal mean winds. However, the vertical structure of DW1 amplitudes shown in Figure 8d does not peak at the nudging boundary, as they do in Figure 11c; rather, they peak around $1\text{--}2 \times 10^{-4} \text{ hPa}$ with values ranging between 5 and 20 m/s. Figure 11c shows peak DW1 zonal wind amplitudes approximately at the nudging boundary that then decrease, until the in situ DW1 dominates. Comparison between Figures 8d and 11c indicates that the vertical structure of DW1 is altered by increasing G in the TIME-GCM.

In general, the results presented in Figure 11 indicate that increasing (decreasing) the relaxation factor (relaxation time) causes the dynamical fields simulated using the 4D Tendency nudging scheme to approach those simulated using the SD nudging schemes. (An intermediate case of only increasing G by ~ 5 is consistent with this and shown as Figure S7 in

Given that model relaxation time decreases as G increases and that the results presented in section 4.1 using increased G in our 4D Tendency nudging simulations reproduces MLT and TI structures similar to those simulated using SD_{zm} and SD_{full} nudging, it is useful to compare the SD_{zm} , SD_{full} , and 4D Tend simulations using the same model relaxation time. A simple relationship equating α , G , and Δt can be deduced such that

$$\alpha = G\Delta t. \quad (6)$$

From equation (6), $\alpha = 1$ is equivalent to a $G = 3.33 \times 10^{-2} \text{ s}^{-1}$, assuming a Δt of 30 s. Conversely, a G of $1.5 \times 10^{-4} \text{ s}^{-1}$ results in an $\alpha = 0.0045$, assuming a Δt of 30 s. For reference, recently performed SD-WACCM and SD-WACCM-X simulations reported on by Smith, Pedatella, et al. (2017) and Sassi et al. (2013) used α s of 0.001 and 0.0083, respectively.

Figure 13 shows the zonal mean climatological zonal winds and DW1 zonal wind amplitudes from TIME-GCM simulations employing the SD_{zm} (a, c, and e) and SD_{full} (b, d, and f) methods, with an $\alpha = 0.0045$. The most striking change is depicted in Figures 13a and 13b, as low-latitude zonal mean climatological zonal winds smoothly transition across the nudging boundary. This smooth vertical gradient in zonal mean zonal winds is a consequence of smoothly varying tendency terms in the zonal mean zonal momentum equation. Specifically, eastward GWD values are $\sim 50 \text{ m}\cdot\text{s}^{-1}\cdot\text{day}^{-1}$ at their peak when α is reduced, as opposed to $\sim 200 \text{ m}\cdot\text{s}^{-1}\cdot\text{day}^{-1}$ in the SD_{zm} and SD_{full} Base Cases (with $\alpha = 1$, represented by the cyan line), closer to the 4D Tend case seen in Figures 4 and 11. Other tendency terms including both horizontal and vertical advection and vertical viscosity have much smaller and smoother vertical gradients in Figures 13c and 13d. DW1 propagates uninhibited across the nudging boundary and peaks around $1\text{--}2 \times 10^{-4} \text{ hPa}$, instead of at the nudging boundary, similar to the 4D Tend simulations with G of $1.5 \times 10^{-4} \text{ s}^{-1}$. Furthermore, SD_{full} with reduced α and 4D Tend simulations with weak G look almost identical in terms of zonal mean climatological winds, zonal wind tendencies, and DW1 amplitudes suggesting that using SD nudging and 4D Tendency nudging can act to drive model dynamics to numerically similar solutions, assuming that the data used to constrain model dynamics and the model relaxation times are equivalent.

Reducing α (i.e., increasing the model relaxation time) also improves SD_{zm} and SD_{full} simulated mean $N_m F_2$ in TIME-GCM (see Figure S9 in the supporting information). On average, decreasing α to 0.0045 leads to a $\sim 10\text{--}35\%$ increase in $N_m F_2$ at low and middle magnetic latitudes, with SD_{full} zonal and daily mean $N_m F_2$ morphology more closely resembling 4D Tend Base Case TIME-GCM simulated (i.e., weak G) and observed COSMIC (Lin et al., 2013) $N_m F_2$. This is a direct result of less horizontal and vertical transport/mixing in the MLT region, leading to more O (and thus O^+) in the thermosphere (ionosphere).

Figures 13 and S9 clearly demonstrate that reducing α in our SD nudging TIME-GCM simulations ameliorates the sharp vertical gradients in low-latitude zonal mean zonal winds and leads to improved $N_m F_2$. As discussed by Jeuken et al. (1996), the reason for these sharp vertical gradients is related to model relaxation time and parameterized physics in the model. In the TIME-GCM, a key parameterized quantity is GWD and, in the absence of nudging, is in balance with other large-scale dynamical tendencies (e.g., advection, pressure gradient, and Coriolis forces) that determine the large-scale wind and temperature (i.e., large-scale winds and temperatures are utilized to calculate the gravity wave propagation conditions for a parameterized spectrum of gravity waves). Therefore, the relaxation term presented in equations (1) and (3) forces the modeled zonal wind (or meridional wind and temperature) toward the observed state while simultaneously hindering the parameterized model physics in reaching a balanced solution with this new model state. Jeuken et al. (1996) state that this issue is analogous to the model spin-up problem in numerical weather prediction. The spin-up problem occurs when the model is relaxed to observations every model time step, as is the case in the SD_{zm} and SD_{full} techniques. As a result, the SD_{zm} and SD_{full} implementations of the SD nudging approach never allow the TIME-GCM time to rectify the initial imbalance in model physics between dynamical and parameterized quantities (i.e., the model is in continuous spin-up since the relaxation time and model time for integration or time step are equal). Our different 4D Tend experiments further elucidate this spin-up problem in the SD_{zm} and SD_{full} cases, as GWD and the artificial tendency term increase in magnitude as G increases (or model relaxation time decreases).

Although not implemented or investigated in this study, another possibility for coupling a lower/middle atmospheric model with an upper atmospheric model is by constraining dynamical model fields in spectral space. Such a technique developed for global dynamic downscaling was recently described by Schubert-Frisius

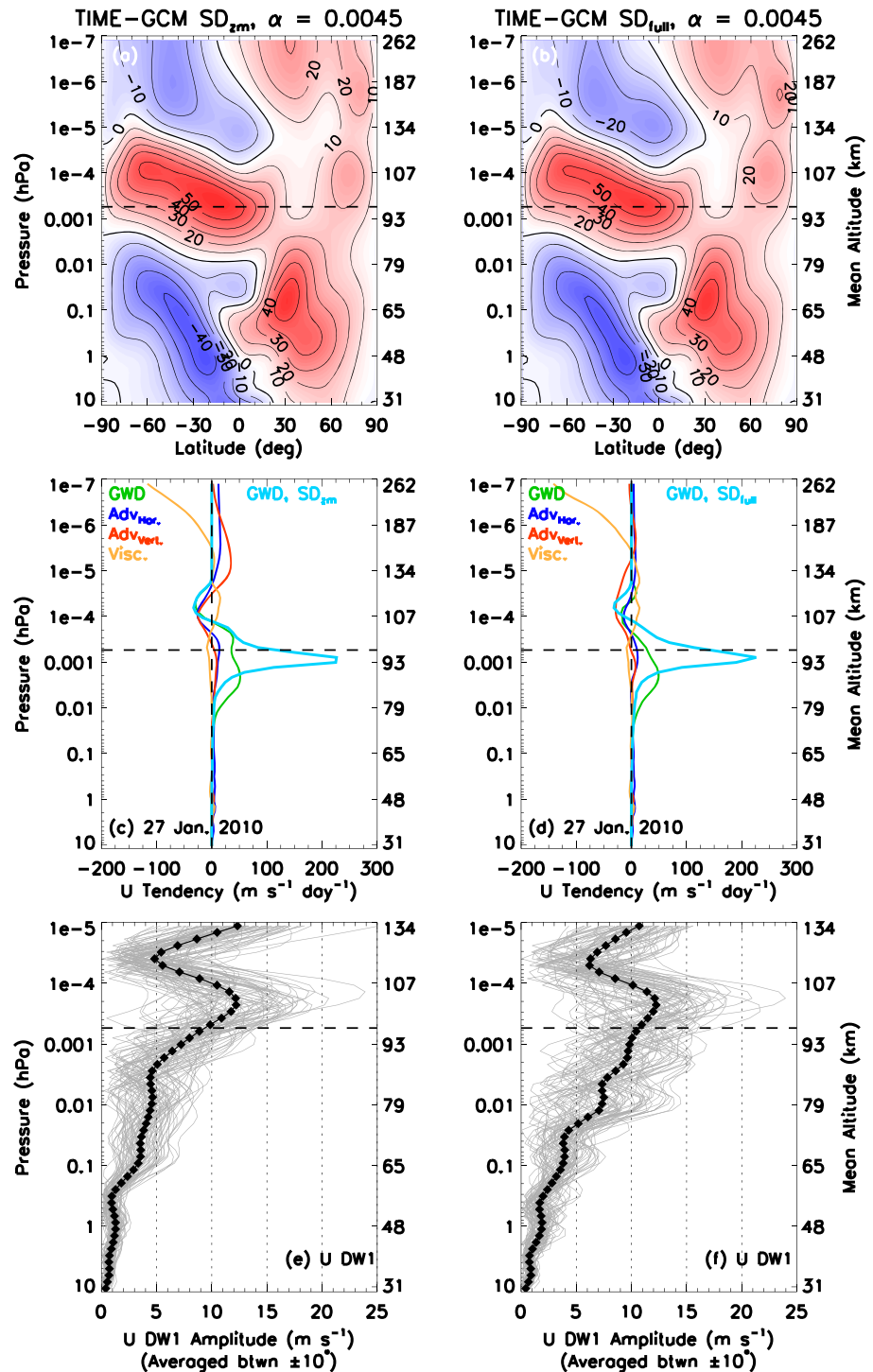


Figure 13. Same as Figure 11 except that Figures 13a, 13c, and 13e and Figures 13b, 13d, and 13f are from the simulations using the SD_{zm} and SD_{full} nudging approaches with $\alpha = 0.0045$, respectively. The tendencies shown in Figures 13c and 13d include GWD (green), horizontal advection ($Adv_{Hor.}$, blue), vertical advection ($Adv_{Ver.}$, red), vertical viscosity (Visc., orange), and GWD from the SD_{zm} and SD_{full} simulations with $\alpha = 1$, or the SD_{zm} or SD_{full} Base Case (GWD, cyan). The bold dashed line indicates where $\zeta = 0$, below (above) which the TIME-GCM is constrained (free running). TIME-GCM = thermosphere-ionosphere-mesosphere-electrodynamics general circulation model; SD = specified dynamics; GWD = gravity wave drag.

et al. (2017). Better coupling between numerical models of different resolution and different physical parameterizations without the generation of spurious numerical artifacts might be achieved in spectral space. This approach allows for nudging of a lower-resolution model by a higher-resolution analysis field, or a high-resolution simulation by a lower resolution analysis.

5. Summary and Conclusions

The results presented herein offer a new methodology for constraining the lower and middle atmospheric dynamics in an upper atmosphere general circulation via 4D Tendency nudging. The present work also demonstrates that although the widely-used SD nudging and the newly implemented 4D Tendency nudging techniques are conceptually different, they can produce approximately equivalent TI responses to SSW forcing, assuming that the nudging parameters are consistent between the two. Using a set of numerical experiments from the TIME-GCM constrained by NAVGEM-HA horizontal winds and neutral temperatures in the stratosphere and mesosphere, we performed a case study of the 2010 SSW period to gain insight into the differential effects SD and 4D Tendency nudging schemes have on resolving MLT and TI dynamics and composition.

All the schemes reproduced the general behavior of the large-scale mean flow at high latitudes, as well as the behavior of PW1. However, at tropical latitudes important differences in the winds and tides were seen that led to differences in neutral and ion composition. Specifically,

1. A sharp vertical mean zonal wind gradient and accompanying strong eastward mean zonal wind jet is induced in the SD_{zm} and SD_{full} simulations at low latitudes surrounding the nudging boundary that is not present in the 4D Tend simulations. These sharp vertical gradients and strong eastward mean zonal winds at low latitudes in the SD_{zm} and SD_{full} cases resulted from strong eastward GWD values near the nudging boundary, a consequence of forcing the TIME-GCM away from its inherent climatology to NAVGEM-HA zonal winds too strongly (Figure 5). Guided by the 4D Tendency nudging scheme employed herein, increasing the model relaxation time in the SD_{zm} and SD_{full} TIME-GCM cases led to improved smooth vertical mean zonal wind gradients and balance of model mean zonal wind tendency terms.
2. The different nudging schemes led to differing migrating and nonmigrating tidal signatures. Mean and daily low-latitude DW1 zonal wind amplitudes in the SD_{zm} and SD_{full} TIME-GCM simulations exhibited sharp vertical gradients at ~ 96 km, yielding amplitudes that were too large (Figures 8b and 8c) and not present in the 4D Tend simulations. These large DW1 zonal wind amplitudes resulted from the sharp vertical gradients in the zonal mean zonal winds. The 4D Tend TIME-GCM simulated DW1 temperature amplitudes (Figure 8h) compared well with previously reported SABER measurements at low latitudes reported by Akmaev et al. (2008) and Zhang et al. (2010a, 2010b). Fewer differences between the three simulations were seen with the SW2 and SW1 temperature amplitudes, with the SD_{zm} simulation producing the strongest SW2 and SW1 absolute amplitudes (Figure 9). Stronger SW2 amplitudes in the SD_{zm} simulation compared with the SD_{full} and 4D Tend simulations arise because SD_{zm} only constrained the zonal mean fields, as opposed to the full fields (i.e., zonal means plus wave perturbations). The sensitivity of SW2 to nudging technique is an important consideration for future model users interested in understanding this wave perturbations influence on TI system dynamics, electrodynamics, and composition.
3. The sharp enhancements in mean and tidal downward dynamical transport above the nudging boundary in the SD_{zm} and SD_{full} simulations likely caused greater downward mixing and hence lower abundances of [O] compared with the 4D Tend simulations (Figure 10). This resulted in daytime (and nighttime) median $N_m F_2$ values from SD_{zm} and SD_{full} simulations that were too low compared to 4D Tend simulations and COSMIC observations (Figures 10 and S6).
4. Regardless of whether the 4D tendency or SD nudging approach is used, selecting the appropriate nudging parameters that produce the proper relaxation time is a critical issue. Both Jeuken et al. (1996) and Telford et al. (2008) also reached this same conclusion, except when implementing nudging in different lower atmospheric GCMs. Specifically, the choice of relaxation factor G in the 4D Tendency nudging scheme and the small parameter α in the SD nudging scheme is extremely important to accurately reproducing SSW-driven phenomena in the TI system (see Figures 11–13). Ultimately, 4D Tendency and SD schemes can be reconciled by varying G and α , such that when constraining data sets and nudging parameters (i.e., G and α) are equivalent, 4D Tendency and SD nudging reproduce almost analogous TI variability in our simulations. That said, stronger coupling (i.e., higher G and α values) will better resolve shorter-frequency fluctuations

up to the boundary of highest constraint but may have unintended side effects in the free-running model domain (e.g., the upper TI). Consequently, choosing the optimal G and α are model dependent and to some extent phenomenon specific.

Although the above assessment of different nudging techniques was performed for middle and upper atmospheric conditions specific to the 2010 SSW period simulated in the NCAR TIME-GCM, our findings illustrate the type of model sensitivity expected when using different methods to constrain stratospheric and mesospheric dynamics in an upper atmosphere GCM. Additionally, the constraining techniques and analysis presented herein specific to the 2010 SSW period have wider applications, including usage in other whole atmosphere general circulation modes and chemistry-climate models that extend into the MLT. Forecasting space weather driven by SSWs represents a modeling benchmark in Earth system science, because SSWs can be predicted a few days in advance by lower and middle atmosphere forecast systems (e.g., Kim et al., 2011; Kim & Flatau, 2010). Thus, any model that seeks to forecast or analyze the short-term variability in the TI system should evaluate the implementation of various nudging techniques and understand the systematic impacts these could have in accurately forecasting (e.g., via ensembles Smith, Pedatella, et al., 2017) and/or reproducing short-term TI variability.

Certainly, there are other considerations in constraining model physics. For example, Sassi et al. (2018) demonstrated that varying the altitude over which a whole atmosphere model is constrained via nudging can result in profound differences in MLT constituent transport. Also, equations (1) and (3) clearly indicate that when implementing nudging in an atmospheric model, differences among different reanalysis/data products will also play a role in driving different dynamical solutions. The relative importance between different reanalysis/data products used to constrain, the vertical domain constrained, and underlying constraining approach will ultimately determine the differences between any set of numerical experiments. Furthermore, the extent to which any one of these three constraining criteria will produce different model solutions will vary between models and the atmospheric regions they are designed to simulate.

Nonetheless, we recommend that the middle and upper atmospheric modeling community strongly consider utilizing 4D Tendency nudging as an option for constraining the dynamical model fields or at the very least to compliment already implemented SD nudging approaches. In addition to constraining model dynamical fields, it is important to note that the 4D Tendency nudging approach adds the momentum (or mass) differences between the model and observed fields as a source term to the conservation equations at each time step; meaning, the model relaxes and tracks observed conditions while maintaining physical self-consistency, including nonlinear feedbacks. Finally, 4D Tendency nudging provides valuable insight into the model parameters that contribute to data-model differences and thus is important to future improvements of middle and upper atmospheric models.

Acronyms

3DVAR	= Three-dimensional variational
4DVAR	= Four-dimensional variational
4D Tend	= 4D Tendency nudging scheme described in this paper
COSMIC	= Constellation Observing System for Meteorology, Ionosphere, and Climate
DA	= Data assimilation
ECMWF	= European Centre for Medium-Range Weather Forecasts
GEOS-5	= Goddard Earth Observing System Data Assimilation System Version 5
GSWM	= Global Scale Wave Model
MLT	= Mesosphere and lower thermosphere
NAVDAS-AR	= NRL Atmospheric Variational Data Assimilation System-Accelerated Representer
NAVEM-HA	= Navy Global Environmental Model a high-altitude version
NCAR	= National Center for Atmospheric Research
NOGAPS-ALPHA	= Navy Operational Global Atmospheric Prediction System-Advanced Level Physics High Altitude forecast model
NRL	= U.S. Naval Research Laboratory
NRLMSISE00	= NRL Mass Spectrometer Incoherent Scatter Radar Extended version 2000
SABER	= Sounding of the Atmosphere using Broadband Emission Radiometry
SD	= Specified dynamics

SD_{full} = Specified dynamics nudging scheme employed in J. C. Wang et al. (2017)
SD_{zm} = Specified dynamics nudging scheme employed in Maute et al. (2015)
SSW = Sudden stratospheric warming
TI = Thermosphere-ionosphere
TIDI = TIMED doppler interferometer
TIE-GCM = Thermosphere-ionosphere-electrodynamics general circulation model
TIME-GCM = Thermosphere-ionosphere-mesosphere-electrodynamics general circulation model
TIMED = Thermosphere Ionosphere Mesosphere Energetics and Dynamics
WACCM = Whole Atmosphere Community Climate Models
WACCM-X = Whole Atmosphere Community Climate model with thermosphere and ionosphere extension

Acknowledgments

The authors would like to thank two anonymous reviewers whose comments significantly improved this work. This work was supported by the NASA Heliophysics Supporting Research (HSR) Program through interagency agreement NNN17AE69I to the U.S. Naval Research Laboratory, and by the Chief of Naval Research. This work was performed while M. Jones held an NRL Karles Fellowship. J. P. M. acknowledges support from NASA grant NNN13AV95I. A. M. is supported by NASA grant X13AF77G. The authors are also grateful to Manbharat Dhadly and John Emmert for helpful discussions, as well as Nicholas Pedatella for thoughtful review of this manuscript prior to submission. Computational resources for this work were provided by the U.S. Department of Defense (DoD) High Performance Computing Modernization Program (HPCMP). The TIME-GCM code is made available by contacting the National Center for Atmospheric Research, and the model output produced herein is reproducible from the TIME-GCM source code following the discussion and implementation of the nudging schemes described mathematically in section 2. NAVGEM-HA inputs used to constrain the stratosphere and mesosphere of the TIME-GCM simulations performed herein are available at <https://map.nrl.navy.mil/map/pub/nrl/james2018/> in netCDF format. Daily NCAR TIME-GCM outputs in netCDF format from this study are archived on the DoD HPCMP long-term storage system. NCAR is sponsored by the National Science Foundation. Any opinions, findings, and conclusions or recommendations expressed in this material are those of the author(s) and do not necessarily reflect the views of the National Science Foundation.

References

- Adams, J. C., & Swartrauber, P. N. (1999). SPHEREPACK 3.0: A model development facility. *Monthly Weather Review*, 127(8), 1872–1878. [https://doi.org/10.1175/1520-0493\(1999\)127<1872:SAMDf>2.0.CO;2](https://doi.org/10.1175/1520-0493(1999)127<1872:SAMDf>2.0.CO;2)
- Akmaev, R. A. (2011). Whole atmosphere modeling: Connecting terrestrial and space weather. *Reviews of Geophysics*, 49, RG4004. <https://doi.org/10.1029/2011RG000364>
- Akmaev, R. A., Fuller-Rowell, T. J., Wu, F., Forbes, J. M., Zhang, X., Anghel, A. F., et al. (2008). Tidal variability in the lower thermosphere: Comparison of Whole Atmosphere Model (WAM) simulations with observations from TIMED. *Geophysical Research Letters*, 35, L03810. <https://doi.org/10.1029/2007GL032584>
- Anthes, R. A., Bernhardt, P. A., Chen, Y., Cucurull, L., Dymond, K. F., Ector, D., et al. (2008). The COSMIC/FORMOSAT-3 mission: Early results. *Bulletin of the American Meteorological Society*, 89(3), 313–334. <https://doi.org/10.1175/BAMS-89-3-313>
- Burns, A. G., Solomon, S. C., Wang, W., Qian, L., Zhang, Y., & Paxton, L. J. (2012). Daytime climatology of ionospheric N_mF_2 and h_mF_2 from COSMIC data. *Journal of Geophysical Research*, 117, A09315. <https://doi.org/10.1029/2012JA017529>
- Butler, A. H., Seidel, D. J., Hardiman, S. C., Butchart, N., Birner, T., & Match, A. (2015). Defining sudden stratospheric warmings. *Bulletin of the American Meteorological Society*, 96(11), 1913–1928. <https://doi.org/10.1175/BAMS-D-13-00173.1>
- Chang, L. C., Palo, S. E., & Liu, H.-L. (2009). Short-term variation of the $s = 1$ nonmigrating semidiurnal tide during the 2002 stratospheric sudden warming. *Journal of Geophysical Research*, 114, D03109. <https://doi.org/10.1029/2008JD010886>
- Chau, J. L., Goncharenko, L. P., Fejer, B. G., & Liu, H. L. (2011). Equatorial and low latitude ionospheric effects during sudden stratospheric warming events. In *2011 URSI General Assembly and Scientific Symposium* (pp. 1–1). <https://doi.org/10.1109/URSIGASS.2011.6050931>
- Codrescu, S. M., Codrescu, M. V., & Fedrizzi, M. (2018). An ensemble Kalman filter for the thermosphere-ionosphere. *Space Weather*, 16, 57–68. <https://doi.org/10.1002/2017SW001752>
- Eckermann, S. D., Hoppel, K. W., Coy, L., McCormack, J. P., Siskind, D. E., Nielsen, K., et al. (2009). High-altitude data assimilation system experiments for the northern summer mesosphere season of 2007. *Journal of Atmospheric and Solar-Terrestrial Physics*, 71(3), 531–551. <https://doi.org/10.1016/j.jastp.2008.09.036>
- Emery, B., Roble, R., Ridley, E., Richmond, A., Knipp, D., Crowley, G., et al. (2012). Parameterization of the ion convection and the auroral oval in the NCAR thermosphere general circulation models (Technical Report). Boulder, CO: National Center for Atmospheric Research. <https://doi.org/10.5065/D6N29TXZ>
- England, S. L. (2012). A review of the effects of non-migrating atmospheric tides on the Earth's low-latitude ionosphere. *Space Science Reviews*, 168(1), 211–236. <https://doi.org/10.1007/s11214-011-9842-4>
- Evans, D. S. (1987). Global statistical patterns of auroral phenomena. In Y. Kamide & R. A. Wolf (Eds.), *Proceedings of the Symposium on Quantitative Modeling of Magnetospheric-Ionospheric Coupling Processes* (pp. 325–330). Kyoto, Japan: Kyoto Sangyo University.
- Fang, T.-W., Fuller-Rowell, T., Akmaev, R., Wu, F., Wang, H., & Anderson, D. (2012). Longitudinal variation of ionospheric vertical drifts during the 2009 sudden stratospheric warming. *Journal of Geophysical Research*, 117, A03324. <https://doi.org/10.1029/2011JA017348>
- Forbes, J. M., Bruinsma, S. L., Zhang, X., & Oberheide, J. (2009). Surface-exosphere coupling due to thermal tides. *Geophysical Research Letters*, 36, L15812. <https://doi.org/10.1029/2009GL038748>
- Forbes, J. M., Roble, R. G., & Fesen, C. G. (1993). Acceleration, heating, and compositional mixing of the thermosphere due to upward propagating tides. *Journal of Geophysical Research*, 98(A1), 311–321. <https://doi.org/10.1029/92JA00442>
- Forbes, J. M., & Vincent, R. A. (1989). Effects of mean winds and dissipation on the diurnal propagating tide: An analytic approach. *Planetary and Space Science*, 37(2), 197–209. [https://doi.org/10.1016/0032-0633\(89\)90007-X](https://doi.org/10.1016/0032-0633(89)90007-X)
- Fuller-Rowell, T. J., Minter, C. F., & Codrescu, M. V. (2004). Data assimilation for neutral thermospheric species during geomagnetic storms. *Radio Science*, 39, RS1503. <https://doi.org/10.1029/2002RS002835>
- Funke, B., López-Puertas, M., Bermejo-Pantaleón, D., García-Comas, M., Stiller, G. P., von Clarmann, T., et al. (2010). Evidence for dynamical coupling from the lower atmosphere to the thermosphere during a major stratospheric warming. *Geophysical Research Letters*, 37, L13803. <https://doi.org/10.1029/2010GL043619>
- Goncharenko, L. P., Coster, A. J., Plumb, R. A., & Domeisen, D. I. V. (2012). The potential role of stratospheric ozone in the stratosphere-ionosphere coupling during stratospheric warmings. *Geophysical Research Letters*, 39, L08101. <https://doi.org/10.1029/2012GL051261>
- Goncharenko, L. P., Hsu, V. W., Brum, C. G. M., Zhang, S.-R., & Fentzke, J. T. (2013). Wave signatures in the midlatitude ionosphere during a sudden stratospheric warming of January 2010. *Journal of Geophysical Research: Space Physics*, 118, 472–487. <https://doi.org/10.1029/2012JA018251>
- Hagan, M. E., & Forbes, J. M. (2002). Migrating and nonmigrating diurnal tides in the middle and upper atmosphere excited by tropospheric latent heat release. *Journal of Geophysical Research*, 107(D24), 4754. <https://doi.org/10.1029/2001JD001236>
- Hagan, M. E., & Forbes, J. M. (2003). Migrating and nonmigrating semidiurnal tides in the upper atmosphere excited by tropospheric latent heat release. *Journal of Geophysical Research*, 108(A2), 1062. <https://doi.org/10.1029/2002JA009466>
- Hagan, M. E., Häusler, K., Lu, G., Forbes, J. M., & Zhang, X. (2015). Upper thermospheric responses to forcing from above and below during 1–10 April 2010: Results from an ensemble of numerical simulations. *Journal of Geophysical Research: Space Physics*, 120, 3160–3174. <https://doi.org/10.1002/2014JA020706>

- Heelis, R. A., Lowell, J. K., & Spiro, R. W. (1982). A model of the high-latitude ionospheric convection pattern. *Journal of Geophysical Research*, 87(A8), 6339–6345. <https://doi.org/10.1029/JA087iA08p06339>
- Hogan, T. F., Liu, M., Ridout, J. A., Peng, M. S., Whitcomb, T. R., Ruston, B. C., et al. (2014). The Navy Global Environmental Model. *Oceanography*, 27, 116–125.
- Jeuken, A. B. M., Siegmund, P. C., Heijboer, L. C., Feichter, J., & Bengtsson, L. (1996). On the potential of assimilating meteorological analyses in a global climate model for the purpose of model validation. *Journal of Geophysical Research*, 101(D12), 16,939–16,950. <https://doi.org/10.1029/96JD01218>
- Jin, H., Miyoshi, Y., Pancheva, D., Mukhtarov, P., Fujiwara, H., & Shinagawa, H. (2012). Response of migrating tides to the stratospheric sudden warming in 2009 and their effects on the ionosphere studied by a whole atmosphere-ionosphere model GAIA with COSMIC and TIMED/SABER observations. *Journal of Geophysical Research*, 117, A10323. <https://doi.org/10.1029/2012JA017650>
- Jones, M., Emmert, J. T., Drob, D. P., & Siskind, D. E. (2017). Middle atmosphere dynamical sources of the semiannual oscillation in the thermosphere and ionosphere. *Geophysical Research Letters*, 44, 12–21. <https://doi.org/10.1002/2016GL071741>
- Jones, M., Forbes, J. M., & Hagan, M. E. (2014). Tidal-induced net transport effects on the oxygen distribution in the thermosphere. *Geophysical Research Letters*, 41, 5272–5279. <https://doi.org/10.1002/2014GL060698>
- Jones, M., Forbes, J. M., Hagan, M. E., & Maute, A. (2014). Impacts of vertically propagating tides on the mean state of the ionosphere-thermosphere system. *Journal of Geophysical Research: Space Physics*, 119, 2197–2213. <https://doi.org/10.1002/2013JA019744>
- Kim, Y.-J., Campbell, W., & Ruston, B. (2011). Hindcasting the January 2009 arctic sudden stratospheric warming with unified parameterization of orographic drag in NOGAPS. Part II: Short-range data-assimilated forecast and the impacts of calibrated radiance bias correction. *Weather and Forecasting*, 26(6), 993–1007. <https://doi.org/10.1175/WAF-D-10-05045.1>
- Kim, Y.-J., & Flatau, M. (2010). Hindcasting the January 2009 Arctic sudden stratospheric warming and its influence on the Arctic oscillation with unified parameterization of orographic drag in NOGAPS. Part I: Extended-range stand-alone forecast. *Weather and Forecasting*, 25(6), 1628–1644. <https://doi.org/10.1175/2010WAF222421.1>
- Kuhl, D. D., Rosmond, T. E., Bishop, C. H., McLay, J., & Baker, N. L. (2013). Comparison of hybrid ensemble/4DVar and 4DVar within the NAVDAS-AR data assimilation framework. *Monthly Weather Review*, 141(8), 2740–2758. <https://doi.org/10.1175/MWR-D-12-00182.1>
- Lin, C., Lin, J., Chang, L., Chen, W., Chen, C., & Liu, J. (2013). Stratospheric sudden warming effects on the ionospheric migrating tides during 2008–2010 observed by FORMOSAT-3/COSMIC. *Journal of Atmospheric and Solar-Terrestrial Physics*, 103, 66–75. <https://doi.org/10.1016/j.jastp.2013.03.026>
- Lindzen, R. S. (1981). Turbulence and stress owing to gravity wave and tidal breakdown. *Journal of Geophysical Research*, 86(C10), 9707–9714. <https://doi.org/10.1029/JC086iC10p09707>
- Lindzen, R. S., & Hong, S. (1974). Effects of mean winds and horizontal temperature gradients on solar and lunar semidiurnal tides in the atmosphere. *Journal of the Atmospheric Sciences*, 31(5), 1421–1446. [https://doi.org/10.1175/1520-0469\(1974\)031<1421:EOMWAH>2.0.CO;2](https://doi.org/10.1175/1520-0469(1974)031<1421:EOMWAH>2.0.CO;2)
- Liu, H.-L. (2016). Variability and predictability of the space environment as related to lower atmosphere forcing. *Space Weather*, 14, 634–658. <https://doi.org/10.1002/2016SW001450>
- Liu, H.-L., Marsh, D. R., She, C.-Y., Wu, Q., & Xu, J. (2009). Momentum balance and gravity wave forcing in the mesosphere and lower thermosphere. *Geophysical Research Letters*, 36, L07805. <https://doi.org/10.1029/2009GL037252>
- Liu, H.-L., & Roble, R. G. (2002). A study of a self-generated stratospheric sudden warming and its mesospheric-lower thermospheric impacts using the coupled TIME-GCM/CCM3. *Journal of Geophysical Research*, 107(D23), 4695. <https://doi.org/10.1029/2001JD001533>
- Liu, H.-L., Wang, W., Richmond, A. D., & Roble, R. G. (2010). Ionospheric variability due to planetary waves and tides for solar minimum conditions. *Journal of Geophysical Research*, 115, A00G01. <https://doi.org/10.1029/2009JA015188>
- Liu, H. L., Yudin, V. A., & Roble, R. G. (2013). Day-to-day ionospheric variability due to lower atmosphere perturbations. *Geophysical Research Letters*, 40, 665–670. <https://doi.org/10.1002/grl.50125>
- Marsh, D. R. (2011). Chemical-dynamical coupling in the mesosphere and lower thermosphere, in aeronomy of the Earth's atmosphere and ionosphere. In M. Abdu & D. Pancheva (Eds.), *Aeronomy of the Earth's atmosphere and ionosphere, IAGA Special Sopron Book Series* (Vol. 2, pp. 3–17). Dordrecht: Springer. https://doi.org/10.1007/978-94-007-0326-1_1
- Matsuo, T., Fedrizzi, M., Fuller-Rowell, T. J., & Codrescu, M. V. (2012). Data assimilation of thermospheric mass density. *Space Weather*, 10, S05002. <https://doi.org/10.1029/2012SW000773>
- Maute, A., Hagan, M. E., Richmond, A. D., & Roble, R. G. (2014). TIME-GCM study of the ionospheric equatorial vertical drift changes during the 2006 stratospheric sudden warming. *Journal of Geophysical Research: Space Physics*, 119, 1287–1305. <https://doi.org/10.1002/2013JA019490>
- Maute, A., Hagan, M. E., Yudin, V., Liu, H.-L., & Yizengaw, E. (2015). Causes of the longitudinal differences in the equatorial vertical E × B drift during the 2013 SSW period as simulated by the TIME-GCM. *Journal of Geophysical Research: Space Physics*, 120, 5117–5136. <https://doi.org/10.1002/2015JA021126>
- McCormack, J., Hoppel, K., Kuhl, D., de Wit, R., Stober, G., Espy, P., et al. (2017). Comparison of mesospheric winds from a high-altitude meteorological analysis system and meteor radar observations during the boreal winters of 2009–2010 and 2012–2013. *Journal of Atmospheric and Solar-Terrestrial Physics*, 154, 132–166. <https://doi.org/10.1016/j.jastp.2016.12.007>
- McDonald, S., Sassi, F., Tate, J., McCormack, J., Kuhl, D., Drob, D., et al. (2018). Impact of non-migrating tides on the low latitude ionosphere during a sudden stratospheric warming event in January 2010. *Journal of Atmospheric and Solar-Terrestrial Physics*, 171, 188–200. <https://doi.org/10.1016/j.jastp.2017.09.012>
- Mendillo, M., Rishbeth, H., Roble, R. G., & Wroten, J. (2002). Modelling F₂-layer seasonal trends and day-to-day variability driven by coupling with the lower atmosphere. *Journal of Atmospheric and Solar-Terrestrial Physics*, 64(18), 1911–1931. [https://doi.org/10.1016/S1364-6826\(02\)00193-1](https://doi.org/10.1016/S1364-6826(02)00193-1)
- Monge-Sanz, B. M., Chipperfield, M. P., Dee, D. P., Simmons, A. J., & Uppala, S. M. (2013). Improvements in the stratospheric transport achieved by a chemistry transport model with ECMWF (re)analyses: identifying effects and remaining challenges. *Quarterly Journal of the Royal Meteorological Society*, 139(672), 654–673. <https://doi.org/10.1002/qj.1996>
- Oberheide, J., Shiokawa, K., Gurubaran, S., Ward, W. E., Fujiwara, H., Kosch, M. J., et al. (2015). The geospace response to variable inputs from the lower atmosphere: A review of the progress made by Task Group 4 of CAWSES-II. *Progress in Earth and Planetary Science*, 2(1), 2. <https://doi.org/10.1186/s40645-014-0031-4>
- Pawson, S., Stajner, I., Kawa, S. R., Hayashi, H., Tan, W.-W., Nielsen, J. E., et al. (2007). Stratospheric transport using 6-h-averaged winds from a data assimilation system. *Journal of Geophysical Research*, 112, D23103. <https://doi.org/10.1029/2006JD007673>

- Pedatella, N. M., Fang, T. W., Jin, H., Sassi, F., Schmidt, H., Chau, J. L., et al. (2016). Multimodel comparison of the ionosphere variability during the 2009 sudden stratosphere warming. *Journal of Geophysical Research: Space Physics*, 121, 7204–7225. <https://doi.org/10.1002/2016JA022859>
- Pedatella, N. M., & Forbes, J. M. (2010). Evidence for stratosphere sudden warming-ionosphere coupling due to vertically propagating tides. *Geophysical Research Letters*, 37, L11104. <https://doi.org/10.1029/2010GL043560>
- Pedatella, N. M., Fuller-Rowell, T., Wang, H., Jin, H., Miyoshi, Y., Fujiwara, H., et al. (2014). The neutral dynamics during the 2009 sudden stratosphere warming simulated by different whole atmosphere models. *Journal of Geophysical Research: Space Physics*, 119, 1306–1324. <https://doi.org/10.1002/2013JA019421>
- Pedatella, N. M., & Liu, H.-L. (2013). The influence of atmospheric tide and planetary wave variability during sudden stratosphere warmings on the low latitude ionosphere. *Journal of Geophysical Research: Space Physics*, 118, 5333–5347. <https://doi.org/10.1002/jgra.50492>
- Pedatella, N. M., & Liu, H.-L. (2018). The influence of internal atmospheric variability on the ionosphere response to a geomagnetic storm. *Geophysical Research Letters*, 45, 4578–4585. <https://doi.org/10.1029/2018GL077867>
- Pedatella, N. M., Liu, H. L., Marsh, D., Raeder, K., Anderson, J., Chau, J., et al. (2018). Analysis and hindcast experiments of the 2009 sudden stratospheric warming in WACCMX+DART. *Journal of Geophysical Research: Space Physics*, 123, 3131–3153. <https://doi.org/10.1002/2017JA025107>
- Pedatella, N. M., Richmond, A. D., Maute, A., & Liu, H.-L. (2016). Impact of semidiurnal tidal variability during ssws on the mean state of the ionosphere and thermosphere. *Journal of Geophysical Research: Space Physics*, 121, 8077–8088. <https://doi.org/10.1002/2016JA022910>
- Picone, J. M., Hedin, A. E., Drob, D. P., & Aikin, A. C. (2002). NRLMSISE-00 empirical model of the atmosphere: Statistical comparisons and scientific issues. *Journal of Geophysical Research*, 107(A12), 1468. <https://doi.org/10.1029/2002JA009430>
- Qian, L., Burns, A. G., Emery, B. A., Foster, B., Lu, G., Maute, A., et al. (2014). The NCAR TIE-GCM. In J. Huba, et al. (Eds.), *Modeling the ionosphere-thermosphere system*. Chichester, UK: John Wiley. <https://doi.org/10.1002/9781118704417.ch7>
- Richards, P. G., Fennelly, J. A., & Torr, D. G. (1994). EUVAC: A solar EUV flux model for aeronomic calculations. *Journal of Geophysical Research*, 99(A5), 8981–8992. <https://doi.org/10.1029/94JA00518>
- Richmond, A. (1995). Ionospheric electrodynamics. In H. Volland (Ed.), *Handbook of atmospheric electrodynamics* (Vol. 2, pp. 249–290). Boca Raton, FL: CRC Press
- Richmond, A. D., & Maute, A. (2014). Ionospheric electrodynamics modeling. In J. Huba (Ed.), *Modeling the ionosphere-thermosphere system*. Washington, DC: American Geophysical Union, pp. 57–71. <https://doi.org/10.1002/9781118704417.ch6>
- Richmond, A. D., Ridley, E. C., & Roble, R. G. (1992). A thermosphere/ionosphere general circulation model with coupled electrodynamics. *Geophysical Research Letters*, 19(6), 601–604. <https://doi.org/10.1029/92GL00401>
- Rienecker, M. M., Suarez, M. J., Todling, R., Bacmeister, J., Takacs, L., & Liu, H.-C. (2008). The GEOS-5 data assimilation system – Documentation of version 5.0.1, 5.1.0, and 5.2.0. Tech. rep.
- Rishbeth, H., & Mendillo, M. (2001). Patterns of F_2 -layer variability. *Journal of Atmospheric and Solar-Terrestrial Physics*, 63(15), 1661–1680. [https://doi.org/10.1016/S1364-6826\(01\)00036-0](https://doi.org/10.1016/S1364-6826(01)00036-0)
- Roble, R. G. (1995). Energetics of the mesosphere and thermosphere. In R. M. Johnson & T. L. Killeen (Eds.), *The upper mesosphere and lower thermosphere: A review of experiment and theory* (pp. 1–21). Washington, DC: American Geophysical Union. <https://doi.org/10.1029/GM087p0001>
- Roble, R. G. (1996). The NCAR thermosphere-ionosphere-mesosphere-electrodynamics general circulation model (TIME-GCM). In R. W. Schunk (Ed.), *Ionosphere Models, STEP Handbook on Ionospheric Models* (pp. 281–288). Logan, UT: Utah State University.
- Roble, R., & Ridley, E. (1987). An auroral model for the NCAR thermospheric general circulation model (TGCM). *Annales Geophysicae*, 5, 369–382.
- Roble, R. G., & Ridley, E. C. (1994). A thermosphere-ionosphere-mesosphere-electrodynamics general circulation model (time-GCM): Equinox solar cycle minimum simulations (30–500 km). *Geophysical Research Letters*, 21(6), 417–420. <https://doi.org/10.1029/93GL03391>
- Sassi, F., Liu, H.-L., Ma, J., & Garcia, R. R. (2013). The lower thermosphere during the Northern Hemisphere winter of 2009: A modeling study using high-altitude data assimilation products in WACCM-X. *Journal of Geophysical Research: Atmospheres*, 118, 8954–8968. <https://doi.org/10.1002/jgrd.50632>
- Sassi, F., Siskind, D. E., Tate, J. L., Liu, H.-L., & Randall, C. E. (2018). Simulations of the boreal winter upper mesosphere and lower thermosphere with meteorological specifications in SD-WACCM-X. *Journal of Geophysical Research: Atmospheres*, 123, 3791–3811. <https://doi.org/10.1002/2017JD027782>
- Schubert-Frisius, M., Feser, F., von Storch, H., & Rast, S. (2017). Optimal spectral nudging for global dynamic downscaling. *Monthly Weather Review*, 145(3), 909–927. <https://doi.org/10.1175/MWR-D-16-0036.1>
- Siskind, D. E., & Drob, D. P. (2014). Use of NOGAPS-ALPHA as a bottom boundary for the NCAR/TIEGCM (pp. 171–180). American Geophysical Union. <https://doi.org/10.1002/9781118704417.ch15>
- Siskind, D. E., Drob, D. P., Dymond, K. F., & McCormack, J. P. (2014). Simulations of the effects of vertical transport on the thermosphere and ionosphere using two coupled models. *Journal of Geophysical Research: Space Physics*, 119, 1172–1185. <https://doi.org/10.1002/2013JA019116>
- Siskind, D. E., Drob, D. P., Emmert, J. T., Stevens, M. H., Sheese, P. E., Llewellyn, E. J., et al. (2012). Linkages between the cold summer mesopause and thermospheric zonal mean circulation. *Geophysical Research Letters*, 39, L01804. <https://doi.org/10.1029/2011GL050196>
- Smith, A. K. (2012). Global dynamics of the MLT. *Surveys in Geophysics*, 33(6), 1177–1230. <https://doi.org/10.1007/s10712-012-9196-9>
- Smith, A. K., Garcia, R. R., Moss, A. C., & Mitchell, N. J. (2017). The semiannual oscillation of the tropical zonal wind in the middle atmosphere derived from satellite geopotential height retrievals. *Journal of the Atmospheric Sciences*, 74(8), 2413–2425. <https://doi.org/10.1175/JAS-D-17-0067.1>
- Smith, A. K., Pedatella, N. M., Marsh, D. R., & Matsuo, T. (2017). On the dynamical control of the mesosphere-lower thermosphere by the lower and middle atmosphere. *Journal of the Atmospheric Sciences*, 74(3), 933–947. <https://doi.org/10.1175/JAS-D-16-0226.1>
- Solomon, S. C., & Qian, L. (2005). Solar extreme-ultraviolet irradiance for general circulation models. *Journal of Geophysical Research*, 110, A10306. <https://doi.org/10.1029/2005JA011160>
- Song, I.-S., Chun, H.-Y., Jee, G., Kim, S.-Y., Kim, J., Kim, Y.-H., & Taylor, M. A. (2018). Dynamic initialization for whole atmospheric global modeling. *Journal of Advances in Modeling Earth Systems*, 10, 2096–2120. <https://doi.org/10.1029/2017MS001213>
- Stauffer, D. R., & Seaman, N. L. (1990). Use of four-dimensional data assimilation in a limited-area mesoscale model. Part I: Experiments with synoptic-scale data. *Monthly Weather Review*, 118(6), 1250–1277. [https://doi.org/10.1175/1520-0493\(1990\)118<1250:UOFDDA>2.0.CO;2](https://doi.org/10.1175/1520-0493(1990)118<1250:UOFDDA>2.0.CO;2)
- Stauffer, D. R., & Seaman, N. L. (1994). Multiscale four-dimensional data assimilation. *Journal of Applied Meteorology*, 33(3), 416–434. [https://doi.org/10.1175/1520-0450\(1994\)033<0416:MFDFA>2.0.CO;2](https://doi.org/10.1175/1520-0450(1994)033<0416:MFDFA>2.0.CO;2)
- Sutton, E. K. (2018). A new method of physics-based data assimilation for the quiet and disturbed thermosphere. *Space Weather*, 16, 736–753. <https://doi.org/10.1002/2017SW001785>

- Swarztrauber, P. N., & Spatz, W. F. (2000). Generalized discrete spherical harmonic transforms. *Journal of Computational Physics*, 159(2), 213–230. <https://doi.org/10.1006/jcph.2000.6431>
- Telford, P. J., Braesicke, P., Morgenstern, O., & Pyle, J. A. (2008). Technical note: Description and assessment of a nudged version of the new dynamics Unified Model. *Atmospheric Chemistry and Physics*, 8(6), 1701–1712. <https://doi.org/10.5194/acp-8-1701-2008>
- Thayer, J. P., Liu, X., Lei, J., Pilinski, M., & Burns, A. G. (2012). The impact of helium on thermosphere mass density response to geomagnetic activity during the recent solar minimum. *Journal of Geophysical Research*, 117, A07315. <https://doi.org/10.1029/2012JA017832>
- Wang, J. C., Chang, L. C., Yue, J., Wang, W., & Siskind, D. E. (2017). The quasi 2 day wave response in TIME-GCM nudged with NOGAPS-ALPHA. *Journal of Geophysical Research: Space Physics*, 122, 5709–5732. <https://doi.org/10.1002/2016JA023745>
- Wang, H., Fuller-Rowell, T. J., Akmaev, R. A., Hu, M., Kleist, D. T., & Iredell, M. D. (2011). First simulations with a whole atmosphere data assimilation and forecast system: The January 2009 major sudden stratospheric warming. *Journal of Geophysical Research*, 116, A12321. <https://doi.org/10.1029/2011JA017081>
- Wu, Q., & Nozawa, S. (2015). Mesospheric and thermospheric observations of the January 2010 stratospheric warming event. *Journal of Atmospheric and Solar-Terrestrial Physics*, 123, 22–38. <https://doi.org/10.1016/j.jastp.2014.11.006>
- Yamashita, C., Liu, H.-L., & Chu, X. (2010). Responses of mesosphere and lower thermosphere temperatures to gravity wave forcing during stratospheric sudden warming. *Geophysical Research Letters*, 37, L09803. <https://doi.org/10.1029/2009GL042351>
- Yamazaki, Y., Kosch, M. J., & Emmert, J. T. (2015). Evidence for stratospheric sudden warming effects on the upper thermosphere derived from satellite orbital decay data during 1967–2013. *Geophysical Research Letters*, 42, 6180–6188. <https://doi.org/10.1002/2015GL065395>
- Yamazaki, Y., & Richmond, A. D. (2013). A theory of ionospheric response to upward-propagating tides: Electrodynamical effects and tidal mixing effects. *Journal of Geophysical Research: Space Physics*, 118, 5891–5905. <https://doi.org/10.1002/jgra.50487>
- Yigit, E., & Medvedev, A. S. (2015). Internal wave coupling processes in Earth's atmosphere. *Advances in Space Research*, 55(4), 983–1003. <https://doi.org/10.1016/j.asr.2014.11.020>
- Zhang, X., Forbes, J. M., & Hagan, M. E. (2010a). Longitudinal variation of tides in the MLT region: 1. Tides driven by tropospheric net radiative heating. *Journal of Geophysical Research*, 115, A06316. <https://doi.org/10.1029/2009JA014897>
- Zhang, X., Forbes, J. M., & Hagan, M. E. (2010b). Longitudinal variation of tides in the MLT region: 2. Relative effects of solar radiative and latent heating. *Journal of Geophysical Research*, 115, A06317. <https://doi.org/10.1029/2009JA014898>
- Zou, X., Navon, I. M., & Ledimet, F. X. (1992). An optimal nudging data assimilation scheme using parameter estimation. *Quarterly Journal of the Royal Meteorological Society*, 118(508), 1163–1186. <https://doi.org/10.1002/qj.49711850808>